The Pennsylvania State University

The Graduate School

College of Engineering

PEFORMANCE EVALUATION AND OPTIMIZATION OF HIGH POWER 14.5-GHz MINIATURE MICROWAVE ELECTROTHERMAL THRUSTER

A Thesis in

Aerospace Engineering

by

Rohit P. Adusumilli

Submitted in Partial Fulfillment
of the Requirements
for the Degree of

Master of Science

May 2011

The thesis of Rohit P. Adusumilli was reviewed and approved* by the following:

Michael M. Micci
Professor of Aerospace Engineering and Director of Graduate Studies
Thesis Advisor

Sven G. Bilén
Associate Professor of Engineering Design, Electrical Engineering, and Aerospace Engineering

George A. Lesieutre
Professor and Head of Aerospace Engineering

*Signatures are on file in the Graduate School

ABSTRACT

This work discusses the design and testing of a high power 14.5-GHz Miniature Microwave Electrothermal Thruster (MET) currently under development at The Pennsylvania State University. The purpose of the MET program is to develop a functional propulsion device that could be used on-board future spacecraft for functions such as attitude control. The current version of the MET was based on an existing lower power (< 20 watts) version with various modifications. Studies were performed in the areas of antenna design, RF inputs, and dielectric shape. In order to assure high coupling efficiency, the cavity was attached to a network analyzer to measure the absorbed power at various antenna lengths. Results showed that antenna protrusions between 0.3 mm to 0.7 mm resulted in the highest absorbed power and provided the highest coupling efficiency. Second, in order to accommodate the requirement for higher power, the antenna's coaxial RF connector was changed from an SMA to an N-type connector. The N-type connector raised the maximum forward power to 100 W. Finally, due to the high temperatures that would be present at the tip of antenna, the insulating Teflon material surrounding the conductor was removed and replaced with boron nitride.

Hot fire testing using helium as propellant resulted in coupling efficiencies as high as 96%. Theoretical analysis of data showed that the MET achieved a maximum thrust of 11 mN with specific impulse as high as 422 s. Recommendations to further improve the functional power range of the MET are also discussed.

TABLE OF CONTENTS

LIST OF FIGURES

LIST OF TABLES

NOMENCLATURE

a	Speed of sound, m/s
	Cavity radius, m
A	Area, m^2
A^*	Throat area, m^2
A_e	Exit area of the nozzle, m^2
A_{mn}	Amplitude constant
A_z	Magnetics vector potential, HA/m
B_{mn}	Vector potential constant, HA/m
C_d	Discharge Coefficient
c^*	Characteristic velocity, m/s
C_τ	Thrust coefficient
E	Electric field, V/m
F	Force, N
f_{res}	Resonant frequency, Hz
g_e	Gravitational acceleration, m/s^2
H	Magnetic field, A/m
h	Enthalpy, J/kg
	Cavity height, m
p_{0c}	Cold flow chamber pressure, Pa
p_{0h}	Hot fire chamber pressure, Pa
Q	Quality factor
R	Gas constant, J/kg K
T_e	Exit temperature, K
T_{0c}	Cold flow chamber temperature, K
T_{0h}	Hot fire chamber temperature, K
h_0	Total enthalpy, J/kg
h_e	Exit enthalpy, J/kg
I	Impulse, N·s
I_{sp}	Specific impulse, s
J_m	Bessel function
J'_m	First derivative of Bessel function
j	Imaginary constant, $\sqrt{-1}$
M	Mach number
m	Mass, kg
$\dot{m}$	Mass flow rate, kg/s
M_p	Total mass of expelled propellant, kg
P	Momentum, N s
p	Pressure, Pa
p_0	Stagnation pressure, Pa
p_a	Ambient pressure, Pa
p_c	Chamber pressure, Pa
p_e	Exit pressure, Pa
R_s	Surface resistance, Ω
T	Temperature, K
T_0	Stagnation temperature, K
T_c	Chamber temperature, K
u	Velocity, m/s
u_e	Exhaust velocity, m/s
u_{eq}	Equivalent exhaust velocity, m/s
W	Stored energy, J

X_s	Surface reactance, Ω
Z_s	Surface Impedance, Ω
β	Wavenumber
β_ρ	ρ-direction wavenumber
β_{res}	Resonant field wavenumber
β_z	z-direction field wavenumber
γ	Ratio of specific heats
Δ	Change in
ε	Permittivity, F/m
μ	Permeability, H/m
ρ	Density, kg/m^3
ρ_0	Stagnation density, kg/m^3
σ	Conductivity, S/m
τ	Thrust, N
τ_m	Momentum thrust, N
χ_{mn}	Zeros of Bessel function
ω	Field radian frequency, Hz
ω_{res}	Resonant field radian frequency, rad/s

ACKNOWLEDGMENTS

I would like to take this moment to acknowledge all the people that have helped me throughout my graduate school experience. First, I would like to thank Dr. Michael Micci and Dr. Sven Bilén for giving me the opportunity to work on an amazing topic. Their guidance and assistance motivated me to do my very best. The wealth of knowledge and intellect that I have attained during this experience will be of tremendous help in my future. Next, I would like to thank Mr. Robert Capuro and Dr. Vladimir Getman for assisting me with the many equipment related problems I encountered. I would like to thank Mr. Bob Dillon for his tremendous machining skills. Finally, I would like to thank all of my friends and family that supported me all the way through graduate school.

CHAPTER 1

Introduction

Researchers at The Pennsylvania State University have been advancing the Microwave Electrothermal Thruster (MET) for the past two decades. An MET uses microwave energy to create and sustain a free-floating plasma inside an electromagnetic cavity. A propellant gas is then injected into the cavity, which is then heated by the plasma and expelled through a gasdynamic nozzle thereby creating thrust.

This thesis describes the performance evaluation of a high frequency (14.5 GHz), high power MET. Furthermore, this thesis provides background information on space propulsion and relevant information in the field of thermodynamics, fluid mechanics, and electromagnetics as it relates to the operation of MET. Finally, pertinent conclusions are made from the presented data, along with recommendations of future work.

1.1 Space Propulsion

Space propulsion systems are the main source of kinetic energy for spacecraft. They generate a force through the process of accelerating a mass known as propellant. Through the use of Newton's Third Law, when mass is expelled opposite to the desired direction of motion, a reactionary force is applied on the spacecraft known as thrust. Controlling the amount of thrust provides the necessary change in kinetic energy for spacecraft to launch into outer space, perform orbital maneuvers, and travel to other

planets. There are three basic types of space propulsion: chemical, electric, and nuclear. Of these three, the two most commonly used are chemical and electric.

1.1.1 Performance Characterization

Chemical propulsion and electrical propulsion differ from each other when it comes to two main rocket performance parameters: thrust and specific impulse. Chemical propulsion systems provide thrust through the combustion of a fuel–oxidizer combination. The energy released from the chemical reaction is transferred into the fluid to create kinetic energy. This energy is then released through a gasdynamic nozzle creating thrust.

A gasdynamic nozzle in itself can be considered as a mechanical device that converts thermal energy to mechanical energy. It consists of a converging section followed by a diverging section that accelerates a flow past Mach 1. In the converging section, the subsonic gas is accelerated until it reaches the throat. The throat is the point of smallest cross section in the nozzle where the flow reaches Mach 1, at which point the flow is considered to be choked. Past the throat, the supersonic or choked flow is further accelerated in the diverging section. An ideal gasdynamic nozzle is designed such that it produces the maximum amount of thrust possible.

The magnitude of the thrust generated by a chemical rocket can be calculated using the momentum equation,

$$P = mu \tag{1.1}$$

The change in momentum with respect to time can be used to calculate the amount of force generated. Since chemical rockets expel mass to generate momentum, we can express the change in momentum as the change in mass flow times the velocity at which it is expelled. As a result, we obtain the equation for the thrust generated as it relates to change in momentum,

$$\tau_m = \dot{m} u_e \tag{1.2}$$

Furthermore, accounting for the additional source of thrust generated at the nozzle exit area due to the difference in ambient and nozzle exit pressures, we obtain the following thrust equation,

$$\tau = \dot{m} u_e + (P_e - P_a) A_e \tag{1.3}$$

Eqn. 1.3 can be further simplified by defining the equivalent exhaust velocity term.

$$u_{eq} = u_e + \left(\frac{P_e - P_a}{\dot{m}} \right) A_e \tag{1.4}$$

Combining Eqns. 1.3 and 1.4, we can obtain the thrust equation.[1]

$$\tau = \dot{m} u_{\text{eq}} \tag{1.5}$$

A complete thrust equation will have to account for losses that happen inside and outside the spacecraft. These can include time integral loss terms due to gravity and atmospheric drag. Furthermore, losses due to the presence of friction and shockwaves inside the nozzle can affect the amount of thrust generated.

Since thrust is a reactionary force, it is measured in units of newtons (N). Chemical rockets can produce between 0.1 N and 12 MN.[2] Since they generate energy through the process of a chemical reaction, they are limited to the amount of energy

generated from the chemical reaction. As a result, chemical rockets are known to be energy limited.

Electric propulsion systems, on the other hand, draw electrical energy from solar cells or fuel cells. This energy is then used in various manners to heat a propellant and then expel it through a gasdynamic nozzle. Therefore, the maximum thrust available is a function of the amount of power that can be put into the system. Typical amounts of thrust from electric propulsion systems range between 10^{-4} N to 20 N.[2] Compared to chemical propulsion systems, electric propulsion systems do not produce high amounts of thrust; however; they have much higher specific impulse.

Specific impulse is a performance parameter used to describe the efficiency of a propulsion system. It describes the amount of impulse generated per unit mass of propellant with respect to earth's gravity, i.e.,

$$I_{\text{sp}} = \frac{I}{M_p g_e} \tag{1.6}$$

The term impulse per unit mass of propellant can also be called the equivalent exhaust velocity.

$$u_{\text{eq}} = \frac{I}{M_p} \tag{1.7}$$

By substituting Eqn. 1.7 into 1.6 one obtains the following expression for specific impulse.[1]

$$I_{\text{sp}} = \frac{u_{\text{eq}}}{g_e} \tag{1.8}$$

While chemical rockets have specific impulses between 200 s and 465 s, the specific impulses for electric rockets lie between 300 s and 100,000 s.[2] The main advantage of electric propulsion systems is that there is no limit to the amount of electric energy that can be used on a single unit of propellant. However, there are physical limitations to the amount of electrical power that can be generated and stored onboard a spacecraft. An electric propulsion system's ability to accelerate small amounts of propellant to very high exhaust velocities makes them the ideal choice for interplanetary travel. Furthermore, the field of electric propulsion provides for a vast area of research on new ways of optimizing current systems and studies into new systems.

1.1.2 Electric Propulsion

Electric propulsion can be classified into three categories: electrostatic, electromagnetic, and electrothermal. In an electrostatic thruster, the propellant is first ionized through the process of electron bombardment or RF ionization. Next, the ionized particles are accelerated by a static electric field in the direction of motion. Electrostatic thrusters are capable of producing very high exhaust velocities with typical specific impulses ranging between 2000 s to 100,000 s. Common examples of electrostatic thrusters include the ion thruster, colloid thruster, and Hall thruster.[2]

Electromagnetic thrusters use an electric field and a magnetic field to accelerate a plasma. The combination of these fields creates a force called the Lorentz force on the plasma. The specific impulses of these thrusters lie between 1000 s and 10,000 s. Some

examples of an electromagnetic thruster include the magnetoplasmadynamic thruster, pulsed plasma thruster, and pulsed inductive thruster.[2]

Electrothermal thrusters produce thrust in a manner similar to chemical rockets. A cold gas is heated and then exhausted through a gasdynamic nozzle to create thrust. Unlike chemical rockets, the process of heating the gas is through electrical energy. The three most common electrothermal thrusters are resistojet, arcjet, and microwave thrusters. Each thruster uses a different technique for heating the gas. For example, a resistojet passes electrical energy to a heating element inside a resistor to heat the gas. An arcjet uses electrical discharge between a cathode and an anode to heat the gas. Finally, a microwave thruster uses microwave energy to create a plasma. The thermal energy from the plasma is then transferred to the propellant and converted into kinetic energy by passing it through a gasdynamic nozzle. Typical specific impulses of these thrusters range between 500 s and 1000 s.[2]

The MET's ability to create plasma without sacrificing material integrity enables them to have a longer lifespan than other electrothermal thrusters. For example, arcjets can heat the propellant to very high temperatures; however; they can suffer from cathode erosion. Resistojets have physical limitations when it comes to the conductor's material properties. Heating the conductor past its melting point can severely damage the thruster.[2]

1.2 Microwave Electrothermal Thruster Overview

The main reason for research into microwave electrothermal thrusters (METs) is the promise of longer lifespan and higher efficiency compared to other electrothermal thrusters. Although METs have never been operated in space flight, their full potential is being tested in laboratories for possible future space missions.[3]

1.2.1 MET Operational Overview

The main principle behind a working MET is the creation and sustainment of a free-floating plasma. Microwave energy is fed from a waveguide into a cylindrical electromagnetic cavity using an antenna. The cavity consists of two endplates with the nozzle located on one end and the antenna on the other end.

Based on an operational resonant frequency of around 14.5 GHz, the cavity's height and radius are sized such that a transverse magnetic TM^{z}_{011} mode is generated. The TM^{z}_{011} mode generates an electric field in which the highest electric field energy occurs at the endplates of the cavity. Figure 1.1 illustrates the field configuration of the induced transverse magnetic mode.

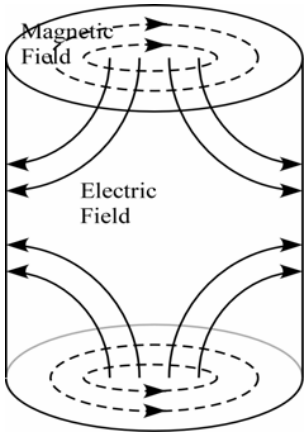

Figure 1.1: Configuration of the electric field and magnetic field in a TM_{011}^{z} mode inside a cylindrical electromagnetic cavity.[3]

These regions of high electric energy densities are required for plasma generation. By shielding the antenna using a ceramic dielectric, the plasma is prevented from being formed at the antenna endplate. Proper calculations of the cavity's height-to-radius ratio as well as the dielectric thickness are required to focus the maximum electrical energy density near the nozzle endplate. The resulting microwave energy creates a free-floating plasma discharge that is axially located and directly upstream of the nozzle.

As illustrated in Figure 1.2, locating the plasma closer to the nozzle provides the most efficient way to transfer heat to the propellant. Due to the high temperature of the plasma, it is also important to locate it away from the cavity walls. This is done by a tangentially fed swirling propellant that creates a radial pressure gradient such that the plasma is centered near the nozzle. The cavity then serves as a pressurized chamber in which the injected propellant is heated using the plasma and quickly exhausted through the gasdynamic nozzle. The plasma is initially generated at low chamber pressure (<3 kPa), but once ignited, it can be sustained at higher chamber pressures.[3]

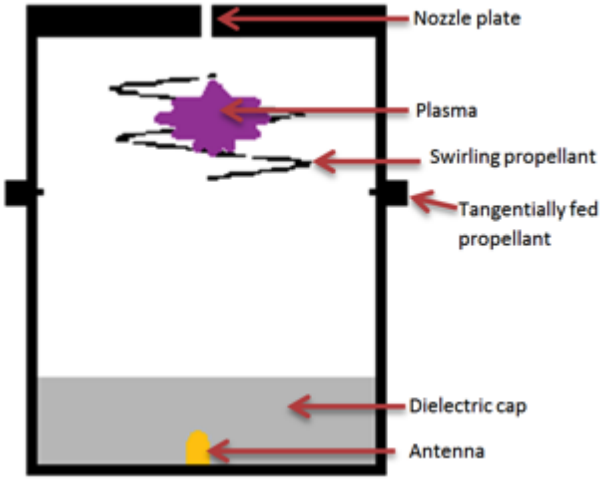

Figure 1.2: Schematic of the MET interior when firing

1.3 Prior Research

The Pennsylvania State University's research into METs first began in 1985 under Micci and Maul. Sullivan[4] created the first working prototype that operated in the TM^{z}_{011} mode at a frequency of 2.45 GHz. His prototype demonstrated the use of swirl-injection propellant to stabilize the plasma, as well as the use of a dielectric separation plate to protect the antenna. Kline[5] advanced the project by being the first to take vacuum chamber thrust measurements of an MET. The data obtained showed that the 2.45-GHz MET attained a maximum thrust of 303 mN while operating in an incident power range between 600 W and 800 W.

Nordling[6] then began research into a high frequency, low power MET. His cavity was scaled down from Sullivan and Kline to operate in the 7.5-GHz range with incident power of about 100 W. Measurements of thrust were taken through a linear variable differential transformer (LVDT) hooked to a suspended pendulum thrust stand. The

displacement in the pendulum by the MET's thrust was recorded by the LVDT. However, due to low thrust-to-weight ratio and lack of resolution from the LVDT, the data acquired were very poor. An inverted pendulum thrust stand was then used in order to increase the resolution. The MET was placed such that its thrust would be exhausted horizontally and any displacement was recorded by the LVDT. The thruster was then tested using helium and nitrogen as propellants. Table 1.1 shows the maximum thrust attained along with its specific impulse and chamber pressure and corresponding mass flow rate.

Table 1.1: Highest performance data attained by Nordling on the 7.5-GHz MET using an inverted pendulum thrust stand.[7]

Propellant	***Max Thrust (mN)***	***Max I_{sp} (sec)***	***Chamber Pressure (psia)***	***Mass Flow (mg/s)***
Helium	7.66	176.3	13.78	4.43
Nitrogen	13.77	130.9	14.65	10.72

The maximum thrust and specific impulse obtained occurred at the same operating conditions. Furthermore, the maximum chamber pressures attained were 14.94 psia for helium and 19.87 psia for nitrogen. By placing the MET horizontally, the buoyancy of the plasma became an issue during nitrogen testing but not during helium testing. Furthermore, the nitrogen plasma was found to be impossible to maintain at a chamber pressure higher than 30 psia.

Following Nordling, Souliez[8] began testing on the 2.4-GHz and the 7.5-GHz MET under low power (<100 W). His results from the low power 2.4-GHz MET concluded that it would be unsuitable for space propulsion applications. The maximum chamber pressure attained was found to be not high enough to produce realistic thrust for

a spacecraft. Therefore, more focus was directed towards the 7.5-GHz MET, which performed well under realistic space conditions. Initial testing with a vertical plasma orientation resulted in chamber pressures as high as 54 psia (373 kPa) for helium, 55 psia (379 psia) for nitrogen, and 7.13 psia (48 kPa) for ammonia.

Further testing for more accurate performance measurements were done using Nordling's setup of an inverted pendulum stand with an LVDT. Under these conditions the plasma was oriented horizontally and helium and nitrogen were used as propellant. Table 1.2 displays the maximum thrust and specific impulse obtained. Further analysis of the data showed that the maximum thrust and the highest specific impulse occurred at two different operating conditions and, as a result, both are shown below. Similar to Nordling, Souliez also experienced buoyancy issues from using the inverted pendulum thrust stand.

Table 1.2: Highest performance data attained by Souliez[8] on the 7.5-GHz MET using an inverted pendulum test stand.

Propellant	***Max Thrust (mN)***	***I_{sp} (sec)***	***Mass Flow (mg/s)***	***Max I_{sp} (sec)***	***Thrust (mN)***	***Mass Flow (mg/s)***
Helium	22	170	12.9	180	19	10.8
Nitrogen	20	75	26.1	92	19	21.6

Roos[9] continued testing on the low power 7.5-GHz MET while using a new vertical deflection thrust stand initially developed by Souliez. The plasma buoyancy issues experienced by Nordling and Souliez resulted in partially inaccurate data and unexpected heating and erosion of the nozzle. In order to eliminate these effects, a new vertical deflection thrust stand was developed using a beam-and-fulcrum concept. The thruster would be aligned vertically downward on one end of a horizontal beam while the

other end was balanced by a lead counterweight. The beam itself would be balanced on a vertical steel knife-edge wedge. An LVDT was placed on the lead weight side of the beam to record any vertical beam deflections. Using this setup, the thrust stand was found to have a resolution of ±1 mN with a LVDT resolution of ±0.5 mN. Hot fire testing of the 7.5-GHz MET while using helium as the propellant resulted in an average thrust of 19.95 mN and maximum I_{sp} of 228 sec. During testing the maximum forward power did not exceed 66 W while plasma coupling efficiencies as high as 99% were attained.

Following Roos, Welander[10] continued testing on the 7.5-GHz MET while focusing on measuring the electromagnetic interference (EMI) produced by the thruster, and also using a completely new momentum trap and strain gage system to measure thrust. The EMI measurements were performed by placing the thruster and all of its operating components inside a sealed anechoic chamber along with a horn antenna. The horn antenna was attached to a spectrum analyzer used to analyze the EMI of the system. The resulting EMI profile showed a sharp single peak at the operating frequency of 7.5 GHz, without any higher harmonics. Since the interference is confined to a single frequency, it could be easily isolated to protect against other communication and scientific components if used onboard a spacecraft. As a result, it was concluded that the MET would require small amount of shielding to make it an electromagnetically quiet propulsion system. Furthermore, Welander's testing involved the use of a new momentum trap system to measure thrust. The purpose of the momentum trap was to measure the amount of force required to bring the momentum of the exhaust gas from the thruster to a complete stop. This was done by hanging the momentum trap from a beam

with an attached strain gage to measure deflections. Proper calibration of the strain gage with known weights was used to convert beam deflection measurements to thrust. Initial testing with the momentum trap produced highly inaccurate data but, it resulted in a system that could be easily repeated.

Clemens[11] continued on Roos' work of using the low power (<63 W) 7.5-GHz MET with the momentum trap. Clemens' testing involved the use of nitrogen as propellant and three different nozzles with varying throat diameters. In addition, the initial momentum trap design was improved upon by increasing the area through which the thruster exhaust stream could escape. This resulted in a momentum trap that was within 90-100% of the theoretical data for a cold flow. However, hot-fire testing again resulted in inaccurate data due to excessive heat transfer between the thruster's exhaust gas, and the thrust stand. Using a converging-diverging nozzle Clemens was able to attain a maximum thrust of 20.8 mN with a specific impulse of 204 s.

In order to meet a new low power requirement a 14.5 GHz MET was designed and tested by Goovaerts[12]. The 14.5-GHz MET operates with a maximum forward power of 20 W while also being considerably smaller and lighter than the 7.5-GHz MET. Initial testing was done using helium as a propellant and maximum input power of 14.3 W. Under these conditions very low chamber pressures were attained with a theoretical maximum thrust of 4.2 mN and a theoretical specific impulse of 197 s. Goovaerts' testing provided a foundation upon which the 14.5-GHz MET could be improved by inputting more power to attain high chamber pressure.

In order to incorporate a space rated TWTA, with an intermediate power range between 100 W and 300 W, a new 8-GHz MET was designed and tested by Blum[13]. The small chamber design along with the higher power meant that the 8-GHz MET could produce higher energy densities than the 2.45-GHz MET and the 7-GHz MET. As a result, the 8-GHz MET could sustain a plasma at higher chamber pressures thereby increasing overall performance. Various parametric studies were also performed involving antenna depth, injector diameter size, and nozzle throat diameter to further optimize the MET. Final testing using ammonia as propellant resulted in a maximum specific impulse that was 33% higher than any other MET using ammonia as propellant.

1.3.1 Thesis Overview

This thesis will continue on the research initially started by Goovaerts on the 14.5-GHz MET. A detailed overview behind the physical theory of a 14.5-GHz MET will be presented in Chapter 2. Chapter 3 contains results from the various optimization studies. The experimental setup and the results will be presented in Chapter 4. Chapter 5 will contain relevant conclusions and suggestions for future work.

CHAPTER 2

Theoretical Background

The physical mechanisms behind the operation of a MET consists of various scientific laws and theories stretching across various fields, the most important of which are fluid mechanics, thermodynamics, and electromagnetics. A rudimentary understanding in these fields is required to develop equations that can model the behavior of a MET. However, deriving complete solutions to the many equations that model the MET is a very complex and time-consuming process. As a result, computer-based physics software is often used to build numerical models and perform simulations. The results of these simulations are then compared with experimental data to improve current models and predict future results.

2.1 Fluid Mechanics and Thermodynamics

The performance of the MET can be characterized using equations derived from fluid mechanics and thermodynamics. Fluid mechanics and thermodynamics are an important prerequisite in the field of propulsion. Most rockets generate thrust through the process of imparting momentum into a fluid, similar to the propellant in a MET. Fluid mechanics provides a vital understanding of how the propellant moves and reacts inside a MET. Thermodynamics provide an understanding of the energy stored within a system. The many thermodynamic properties of a fluid can be derived from the two laws of thermodynamics.[1]

2.1.1 Isentropic Flow Relations

Isentropic flows are commonly used to model ideal processes. An isentropic assumption states that a process can take place from beginning to end without any increase or decrease in entropy.[1] Using the formulated thermodynamic laws the following isentropic flow relation between temperature and pressure can be derived

$$\frac{p_0}{p} = \left(\frac{T_0}{T}\right)^{\frac{\gamma}{\gamma-1}} \tag{2.1}$$

Similar relations can be obtained for density using the perfect gas law

$$\frac{\rho_0}{\rho} = \left(\frac{T_0}{T}\right)^{\frac{1}{\gamma-1}} \tag{2.2}$$

$$\frac{p_0}{p} = \left(\frac{\rho_0}{\rho}\right)^{\gamma} \tag{2.3}$$

Isentropic flows introduce the following terms p_0, T_0, and ρ_0 known as stagnation conditions. A stagnation state can be described as state reached by a fluid if it is brought to rest isentropically. The temperature, pressure and density that would exist at this state are defined as stagnation conditions.

An important parameter commonly used in the field of compressible flows is the Mach number, *M*. It is ratio of the flow velocity, *u*, to the local speed of sound, *a*, and can be expressed as

$$M = \frac{u}{a} \tag{2.4}$$

The local speed of sound is a function of the fluid's specific heat ratio and temperature and therefore gives us the following relationship

$$a = \sqrt{\gamma RT} \tag{2.5}$$

By assuming constant specific heat we can derive the isentropic flow equations for temperature, density, and pressure as function of Mach number, i.e.,

$$\frac{T_0}{T} = 1 + \frac{\gamma - 1}{2} M^2 \tag{2.6}$$

$$\frac{\rho_0}{\rho} = \left(1 + \frac{\gamma - 1}{2} M^2\right)^{\frac{1}{\gamma - 1}} \tag{2.7}$$

$$\frac{p_0}{p} = \left(1 + \frac{\gamma - 1}{2} M^2\right)^{\frac{\gamma}{\gamma - 1}} \tag{2.8}$$

2.1.2 Performance Characteristics

The flow of fluid through an ideal MET nozzle can be modeled as an ideal isentropic process. Using the isentropic flow relations in Section 2.1.1, one can derive the equations for flow velocity and thrust in order to characterize the performance of the MET. First, the conservation of mass equation from fluid mechanics is simplified to obtain the mass flow rate per unit area[1]

$$\frac{\dot{m}}{A} = \rho u \tag{2.9}$$

Combining Eqns. 2.4–2.6, the flow velocity can be expressed as

$$u = M \sqrt{\frac{\gamma RT_0}{1 + \frac{\gamma - 1}{2} M^2}} \tag{2.10}$$

Since the flow inside the chamber is very slow compared to the flow through the nozzle, the stagnation conditions can be referred to as chamber conditions. Replacing the subscript 0 with *c*, we can rewrite the mass per unit area as a function of chamber pressure and temperature.

$$\frac{\dot{m}}{A} = \frac{p_c\sqrt{\gamma}}{\sqrt{RT_c}} M \left(\frac{1}{1 + \frac{\gamma - 1}{2} M^2} \right)^{\frac{\gamma+1}{2(\gamma-1)}} \tag{2.11}$$

Given that the $M = 1$ at the nozzle throat, $A = A^*$, Eqn. 2.11 can be simplified to

$$\frac{\dot{m}}{A^*} = \frac{p_c\sqrt{\gamma}}{\sqrt{RT_c}} \left(\frac{2}{\gamma + 1} \right)^{\frac{\gamma+1}{2(\gamma-1)}} \tag{2.12}$$

Dividing Eqns. 2.12 by 2.11, we can obtain the equation for the area ratio.

$$\frac{A}{A^*} = \frac{1}{M} \left[\frac{2}{\gamma + 1} \left(1 + \frac{\gamma - 1}{2} M^2 \right) \right]^{\frac{\gamma+1}{2(\gamma-1)}} \tag{2.13}$$

Furthermore, by assuming an adiabatic nozzle expansion we can use conservation of energy to obtain an enthalpy relation across the nozzle, where subscript *e* denotes the conditions at the nozzle exit.

$$h_c + \frac{u_c^2}{2} = h_e + \frac{u_e^2}{2} \tag{2.14}$$

However, since the chamber velocity, u_c, is assumed to be zero, Eqn. 2.14 simplifies to

$$\frac{u_e^2}{2} = h_c - h_e = c_p(T_c - T_e) \tag{2.15}$$

Substituting the isentropic flow relations we can derive the equation for the exit flow velocity as

$$u_e = \sqrt{\frac{2\gamma RT_c}{(\gamma-1)}\left[1-\left(\frac{p_e}{p_c}\right)^{\frac{\gamma-1}{\gamma}}\right]} \tag{2.16}$$

Using the thrust equation in Chapter 1, Eqns. 2.12 and 2.16 can be substituted to obtain the following result for thrust

$$\tau = A^* p_c \sqrt{\frac{2\gamma^2}{\gamma-1}\left(\frac{2}{\gamma+1}\right)^{\frac{\gamma+1}{\gamma-1}}\left[1-\left(\frac{p_e}{p_c}\right)^{\frac{\gamma-1}{\gamma}}\right]} + (p_e - p_a)A_e \tag{2.17}$$

For the sake of analysis, it is more convenient to separately describe the performance of the two rocket chamber components, chamber and nozzle. The effectiveness of a combustion chamber can be defined using the characteristic velocity coefficient, c^*, expressed as

$$c^* \equiv \frac{p_0 A^*}{\dot{m}} \tag{2.18}$$

Using Eqn. 2.12 we obtain the equation for characteristic velocity for an ideal rocket, which as it turns out, is mainly a function of chamber temperature.

$$c^* = \sqrt{\frac{1}{\gamma}\left(\frac{\gamma+1}{2}\right)^{\frac{\gamma+1}{\gamma-1}} RT_c} \tag{2.19}$$

The performance of a nozzle is defined using the thrust coefficient, C_τ, defined as

$$C_\tau \equiv \frac{\tau}{p_0 A^*} \tag{2.20}$$

Using Eqn. 2.17 it can be further expanded to

$$C_\tau = \sqrt{\frac{2\gamma^2}{\gamma-1}\left(\frac{2}{\gamma+1}\right)^{\frac{\gamma+1}{\gamma-1}}\left[1-\left(\frac{p_e}{p_c}\right)^{\frac{\gamma-1}{\gamma}}\right]} + \frac{(p_e - p_a)A_e}{p_0 A^*} \qquad \textbf{(2.21)}$$

Combining the two performance coefficients we can obtain the following simplified thrust equation

$$\tau = \dot{m} c^* C_\tau \qquad \textbf{(2.22)}$$

Using Eqns. 2.17 and 1.8 and the recorded mass flow rates, preliminary values of thrust and specific impulse are calculated for cold flow in Chapter 4.

2.1.3 Nozzle Boundary Layer Assumptions

As with any fluid flow, propellant flow through the nozzle is greatly affected by viscous effects near the wall. For large-diameter nozzles these effects are typically small; however, due to the MET nozzle's small diameter, boundary layer restriction problems can arise. The free-stream flow is displaced from the wall due to the presence of a boundary layer, which in turn can reduce the exit area of the nozzle. The changing exit area can affect the chamber temperature values calculated using recorded experimental data for chamber pressure and mass flow rate. To account for these losses, a discharge coefficient is introduced and defined as the ratio of the actual mass flow rate to the theoretical mass flow rate, i.e.,

$$C_d = \frac{\dot{m}_{\text{act}}}{\frac{A^* p_c \sqrt{\gamma}}{\sqrt{RT_c}}\left(\frac{2}{\gamma+1}\right)^{\frac{\gamma+1}{2(\gamma-1)}}} \qquad \textbf{(2.23)}$$

However, due to high temperatures expected inside the chamber during hot fire, it would be impossible to measure the temperature. As a result, using isentropic flow relations the following equation can be used to calculate the chamber temperature under hot fire conditions.

$$T_{0h} = T_{0c}\left(\frac{p_{0h}}{p_{0c}}\right)^2\left(\frac{C_{dh}}{C_{dc}}\right)^2 \quad \textbf{(2.24)}$$

Here the subscripts *c* and *h* refer to cold flow and hot fire conditions, respectively. For this work, however, the nozzle boundary layer restrictions will be ignored and the discharge coefficient will be set to 1 for both cold flow and hot fire conditions. Consequently, the hot fire chamber temperature will only be a function of hot fire chamber pressure and cold flow temperature and chamber pressure, i.e.,

$$T_{0h} = T_{0c}\left(\frac{p_{0h}}{p_{0c}}\right)^2 \quad \textbf{(2.25)}$$

2.2 Electromagnetics

As stated in Chapter 1, an MET uses continuous wave (CW) microwave energy to create and maintain a plasma discharge. The equations governing this process are defined using electromagnetic theory.

2.2.1 Transverse Magnetic (TM^z) Modes

Since the MET uses a cylindrical cavity, it can be considered as a circular waveguide shorted out at the ends with two conducting plates. The cylindrical geometry of the cavity makes it convenient to derive field equations using the cylindrical coordinate system displayed in Figure 2.1.

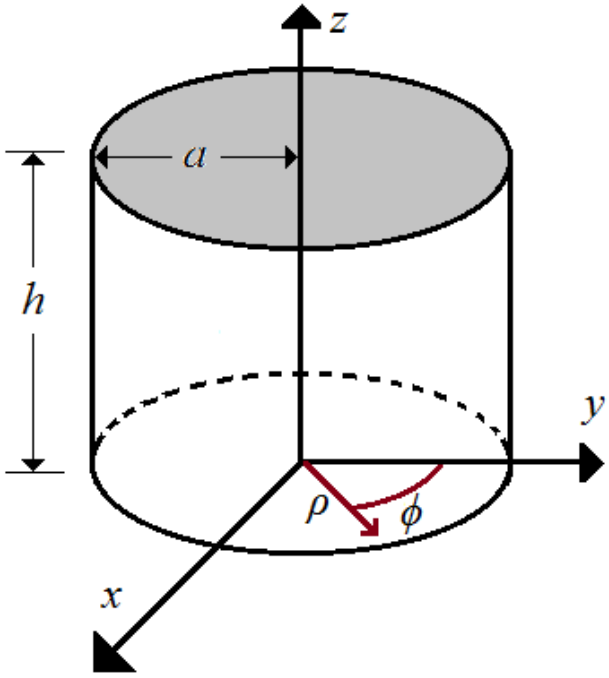

Figure 2.1: Resonant cavity cylindrical coordinate system

The transverse magnetic mode to *z* can be derived by setting the vector potential *A* equal to[14]

$$\mathbf{A} = \hat{a}_z A_z(\rho, \phi, z) \tag{2.26}$$

To satisfy the wave equation, *A* reduces to

$$\nabla^2 A_z(\rho, \phi, z) + \beta^2 A_z(\rho, \phi, z) = 0 \tag{2.27}$$

the solution for which can be written as

$$A_z(\rho,\phi,z) = \left[A_1 J_m(\beta_\rho \rho) + B_1 Y_m(\beta_\rho \rho)\right] \times [C_2 \cos(m\phi) + D_2 \sin(m\phi)]\left[A_3 e^{-j\beta_z z} + B_3 e^{j\beta_z z}\right] \quad \textbf{(2.28)}$$

The resonant wavenumber β, can be solved as a function of radial direction wavenumber and transverse direction wavenumber

$$\beta = \beta_\rho^2 + \beta_z^2 \quad \textbf{(2.29)}$$

The constants of integration in Eqn. 2.28 can be found by applying the following boundary conditions

$$E_\phi(\rho = a.\phi, z) = 0$$
$$E_z(\rho = a.\phi, z) = 0 \quad \textbf{(2.30)}$$

Furthermore, assuming the field is finite everywhere and repeats every 2π radians in the ϕ direction, Eqn. 2.28 reduces to

$$A_z(\rho,\phi,z) = B_{mn} J_m(\beta_\rho \rho)[C_2 \cos(m\phi) + D_2 \sin(m\phi)]e^{-j\beta_z z} \quad \textbf{(2.31)}$$

The equations for the electric field and magnetic field in the ρ, ϕ, and z directions can be written as

$$E_\rho = -j\frac{1}{\omega\mu\epsilon}\frac{\partial^2 A_z}{\partial\rho\partial z} \quad \textbf{(2.32)}$$

$$E_\phi = -j\frac{1}{\omega\mu\epsilon}\frac{1}{\rho}\frac{\partial^2 A_z}{\partial\phi\partial z} \quad \textbf{(2.33)}$$

$$E_z = -j\frac{1}{\omega\mu\epsilon}\left(\frac{\partial^2}{\partial z^2} + \beta^2\right)A_z \quad \textbf{(2.34)}$$

$$H_\rho = \frac{1}{\mu}\frac{1}{\rho}\frac{\partial A_z}{\partial\phi} \quad \textbf{(2.35)}$$

$$H_\phi = -\frac{1}{\mu}\frac{\partial A_z}{\partial \rho} \tag{2.36}$$

$$H_z = 0 \tag{2.37}$$

where μ and ε are the permeability and permittivity, respectively, of the gas inside the MET. Due to the presence of the two end plates, additional boundary conditions can be applied to the E field component in the ϕ direction. First, Eqn. 2.33 can to be expanded to the following form

$$\begin{aligned} E_\phi(\rho,\phi,z) = -jB_{mn}\frac{m\beta_z}{\omega\mu\epsilon}\frac{1}{\rho}J_m(\beta_\rho\rho)[-C_2\sin(m\phi) \\ + D_2\cos(m\phi)] \times [-C_3\sin(\beta_z z) + D_3\cos(\beta_z z)] \end{aligned} \tag{2.38}$$

First, at the bottom ($z = 0$) the following boundary condition can be applied

$$E_\phi(0 \le \rho \le a, 0 \le \phi \le 2\pi, z = 0) = 0 \tag{2.39}$$

leading to

$$\begin{aligned} E_\phi(\rho,\phi,z) = -jB_{mn}\frac{m\beta_z}{\omega\mu\epsilon}\frac{1}{\rho}J_m(\beta_\rho\rho)[-C_2\sin(m\phi) \\ + D_2\cos(m\phi)] \times [-C_3\,(0) + D_3(1)] = 0 \\ D_3 = 0 \end{aligned} \tag{2.40}$$

Next, the boundary condition at $z = h$,

$$E_\phi(0 \le \rho \le a, 0 \le \phi \le 2\pi, z = h) = 0 \tag{2.41}$$

is applied leading to

$$E_\phi(\rho,\phi,z) = jB_{mn}\frac{m\beta_z}{\omega\mu\epsilon}\frac{1}{\rho}J_m(\beta_\rho\rho)[-C_2\sin(m\phi) + D_2\cos(m\phi)][C_3\sin(\beta_z h)] = 0$$
$$\sin(\beta_z h) = 0 \Rightarrow \beta_z h = \sin^{-1}(0) = p\pi \qquad \textbf{(2.42)}$$
$$\beta_z = \frac{p\pi}{h} \qquad p = 0,\quad 1,2,3,\ldots.$$

By substituting the equation for the radial wave number as a function of the zeros of the Bessel function χ_{mn},

$$\beta_\rho = \frac{\chi_{mn}}{a} \qquad m = 0,1,2,3,\ldots \qquad \textbf{(2.43)}$$

the equation for the resonant frequency can be found as

$$\beta_\rho^2 + \beta_z^2 = \left(\frac{\chi_{mn}}{a}\right)^2 + \left(\frac{p\pi}{h}\right)^2 = \beta_{\text{res}}^2 = \omega_{\text{res}}^2\mu\epsilon \qquad \textbf{(2.44)}$$

or through further substitution

$$(f_r)_{mnp}^{\text{TM}^z} = \frac{1}{2\pi\sqrt{\mu\epsilon}}\sqrt{\left(\frac{\chi_{mn}}{a}\right)^2 + \left(\frac{p\pi}{h}\right)^2} \quad m = 0,1,2,3 \qquad \textbf{(2.45)}$$

The final form of the potential function, A_z

$$A_z(\rho,\phi,z) = B_{mnp}J_m(\beta_\rho\rho)[C_2\cos(m\phi) + D_2\sin(m\phi)]\cos(\beta_z z) \qquad \textbf{(2.46)}$$

can be plugged in to Eqns. 2.32–2.37 to derive the complete electric and magnetic field equations for a circular cavity in a TM^z_{011} mode.

$$(f_r)_{011}^{\text{TM}^z} = \frac{1}{2\pi\sqrt{\mu\epsilon}}\sqrt{\left(\frac{\chi_{01}}{a}\right)^2 + \left(\frac{\pi}{h}\right)^2} \qquad \textbf{(2.47)}$$

$$E_\rho = j\frac{B_{011}}{\omega\mu\epsilon}\frac{\pi}{h}\frac{\chi_{01}}{a}J'_0\left(\frac{\chi_{01}}{a}\rho\right)\sin\left(\frac{\pi}{h}z\right) \qquad \textbf{(2.48)}$$

$$E_\phi = 0 \tag{2.49}$$

$$E_z = -j\frac{B_{011}}{\omega\mu\epsilon}\left(\frac{\chi_{01}}{a}\right)^2 J'_0\left(\frac{\chi_{01}}{a}\rho\right)\cos\left(\frac{\pi}{h}z\right) \tag{2.50}$$

$$H_\rho = 0 \tag{2.51}$$

$$H_\phi = -\frac{\chi_{01}}{a}\frac{B_{011}}{\mu}J'_0\left(\frac{\chi_{01}}{a}\rho\right)\cos\left(\frac{\pi}{h}z\right) \tag{2.52}$$

$$H_z = 0 \tag{2.53}$$

For an operational frequency around 14.5 GHz, Eqn. 2.47 was used to calculate an approximate height-to-radius ratio of the cavity.

2.2.2 Quality Factor

An important parameter describing the performance of a resonant cavity is the quality factor, *Q*.[14] It is the ratio of the total energy stored in the cavity, *W*, to the total power dissipated inside the cavity, P_d, at a particular resonant frequency.

$$Q = \frac{\omega_{\text{res}}W}{P_d} \tag{2.54}$$

The total energy stored in the cavity is given by

$$W = \frac{\varepsilon}{2}\iiint_V |\mathbf{E}|^2 dv \tag{2.55}$$

where **E** can be replaced by Eqns. 2.48–2.50 to derive the following equation for the quality factor in the TM^z_{011} mode.

$$W = \frac{\varepsilon}{2}\left(\frac{B_{011}}{\omega\mu\varepsilon}\right)^2\left(\frac{\chi_{01}}{a}\right)^2\int_0^h\int_0^{2\pi}\int_0^a\left[\left(\frac{\pi}{h}\right)^2 J'_0\left(\frac{\chi_{01}}{a}\rho\right)^2\sin^2\left(\frac{\pi}{h}z\right)\right.$$
$$\left. + \left(\frac{\chi_{01}}{a}\right)^2 J_0^2\left(\frac{\chi_{01}}{a}\rho\right)^2\cos^2\left(\frac{\pi}{h}z\right)\right]\rho d\rho d\phi dz \quad \textbf{(2.56)}$$

Through the use of the following Bessel function recurrence relations, Eqn. 2.56 can be evaluated in terms of Bessel functions of the first order.

$$J'_n(x) = \frac{n}{x}J_n(x) - J_{n+1}(x)$$
$$J'_0\left(\frac{\chi_{01}}{a}\rho\right) = -J_1\left(\frac{\chi_{01}}{a}\rho\right) \quad \textbf{(2.57)}$$

Evaluating the integrals leads to the following simplified equation for *W*

$$W = \left(\frac{B_{011}}{\omega\mu\varepsilon}\right)^2\left(\frac{\chi_{01}}{a}\right)^2\left(\frac{\pi\epsilon h a^2}{4}\right)J_1^2(\chi_{01})\left[\left(\frac{\pi}{h}\right)^2 + \left(\frac{\chi_{01}}{a}\right)^2\right] \quad \textbf{(2.58)}$$

By assuming the medium inside the cavity to be lossless, the power dissipated on the cavity's conducting walls can be found by the following equation.

$$P_d = \frac{R_s}{2}\oiint_A |\mathbf{H}|^2 ds$$
$$P_d = \frac{R_s}{2}\left\{\int_0^{2\pi}\int_0^h |\mathbf{H}|^2_{\rho=a} a d\phi dz + 2\int_0^{2\pi}\int_0^a |\mathbf{H}|^2_{z=0}\rho d\rho d\phi\right\} \quad \textbf{(2.59)}$$

where R_s is the real part of the surface impedance Z_s expressed as

$$Z_s = R_s + jX_s = (1+j)\sqrt{\frac{\omega\mu}{2\sigma}} \quad \textbf{(2.60)}$$

By substituting the equations for the magnetic field, Eqn. 2.52, into Eqn. 2.59 the following expression for dissipated power can be obtained

$$P_d = |B_{011}|^2 \frac{R_s}{2\mu^2}\left(\frac{\chi_{01}}{a}\right)^2 \left\{ \int_0^{2\pi} \int_0^{h} J'_0(\chi_{01})^2 \cos^2\left(\frac{\pi}{h} z\right) a d\phi dz \right. \\ \left. + 2 \int_0^{2\pi} \int_0^{a} J'_0\left(\frac{\chi_{01}}{a}\rho\right)^2 \rho d\rho d\phi \right\} \tag{2.61}$$

Evaluating the surface integral leads to the following solution for dissipated power

$$P_d = |B_{011}|^2 \frac{R_s}{2\mu^2}\left(\frac{\chi_{01}}{a}\right)^2 \pi J_1(\chi_{01})^2 (2a^2 + h^2) \tag{2.62}$$

Substituting Eqns. 2.58 and 2.62 into Eqn. 2.54 yields the following equation for *Q*

$$Q = \frac{ha^2}{ha + 2a^2}\left(\frac{\mu}{\varepsilon}\right)^{\frac{1}{4}}\left(\frac{\sigma}{2}\right)^{\frac{1}{2}}\left[\left(\frac{\pi}{h}\right)^2 + \left(\frac{\chi_{01}}{a}\right)^2\right]^{\frac{1}{4}} \tag{2.63}$$

As seen in Eqn. 2.63, the quality factor is a function of the cavity's height and radius as well as the permittivity, permeability, and conductivity of the medium inside the cavity.

2.2.3 Field Equations with Dielectric Insert

A dielectric is insulating material that can modify the electromagnetic wave propagation. The purpose of the dielectric in the MET is to protect the antenna and prevent the formation of plasma near the antenna end. Boron nitride was chosen as the dielectric for the MET due to its ability to withstand high temperatures.

The presence of the dielectric can change the cavity's resonant frequency as well as the field equations.[12] To derive the new equations, the cavity must be split into two regions, gas and dielectric. The region covered by the gas will be denoted by the

subscript g and dielectric region will be denoted by subscript d. As seen in Section 2.2.1, we begin the vector potential and resonant frequency equations for the two regions

$$A_{z,d}(\rho,\phi,z) = B_{mnp,d} J_m(\beta_\rho \rho)\cos(m\phi)\cos\left(\beta_{z,d} z\right)$$
$$\beta_{\mathrm{res},d}^2 = \beta_\rho^2 + \beta_{z,d}^2 = \omega_{\mathrm{res}}^2 \mu_d \epsilon_d \quad \textbf{(2.64)}$$

$$A_{z,g}(\rho,\phi,z) = B_{mnp,g} J_m(\beta_\rho \rho)\cos(m\phi)\cos\left(\beta_{z,g} z - h\right)$$
$$\beta_{\mathrm{res},g}^2 = \beta_\rho^2 + \beta_{z,g}^2 = \omega_{\mathrm{res}}^2 \mu_g \epsilon_g \quad \textbf{(2.65)}$$

By applying similar boundary conditions we obtain the radial E-field component

$$E_{\rho,d} = -j\frac{B_{mnp,d}}{\omega\mu_d\epsilon_d}\beta_\rho\beta_{z,d}\, J'_m\left(\beta_\rho\rho\right)\sin\left(\beta_{z,d} z\right)\cos(m\phi) \quad \textbf{(2.66)}$$

$$E_{\rho,g} = -j\frac{B_{mnp,g}}{\omega\mu_g\epsilon_g}\beta_\rho\beta_{z,g}\, J'_m\left(\beta_\rho\rho\right)\sin\left(\beta_{z,g}(z-h)\right)\cos(m\phi) \quad \textbf{(2.67)}$$

and the magnetic field component in the ϕ direction

$$H_{\phi,d} = -\frac{B_{mnp,d}\,\beta_\rho}{\mu_d}\, J'_m\left(\beta_\rho\rho\right)\cos\left(\beta_{z,d} z\right)\cos(m\phi) \quad \textbf{(2.68)}$$

$$H_{\phi,g} = -\frac{B_{mnp,g}\,\beta_\rho}{\mu_g}\, J'_m\left(\beta_\rho\rho\right)\cos\left(\beta_{z,g}(z-h)\right)\cos(m\phi) \quad \textbf{(2.69)}$$

Since the field components tangential to the gas–dielectric interface are continuous, we can derive the following conditions

$$E_{\rho,d}(z=t) = E_{\rho,g}(z=t) \quad \textbf{(2.70)}$$

$$H_{\phi,d}(z=t) = H_{\phi,g}(z=t) \quad \textbf{(2.71)}$$

where t is the thickness of the dielectric. By substituting Eqns. 2.66–2.69 into the above conditions and cancelling out like terms, we obtain the following expressions

$$\frac{B_{mnp,d}}{\mu_d \epsilon_d}\beta_{z,d}\ \sin\left(\beta_{z,d}t\right) = \frac{B_{mnp,g}}{\mu_g \epsilon_g}\beta_{z,g}\sin\left(\beta_{z,g}(t-h)\right) \quad \textbf{(2.72)}$$

$$\frac{B_{mnp,d}}{\mu_d}\cos\left(\beta_{z,d}t\right) = \frac{B_{mnp,g}}{\mu_g}\cos\left(\beta_{z,g}(t-h)\right) \quad \textbf{(2.73)}$$

Dividing Eqns. 2.72 and 2.73 with each other results in an equation that relates the resonant wavenumber in the *z*-direction for the two regions, i.e.,

$$\frac{\beta_{z,d}}{\varepsilon_d}\tan\left(\beta_{z,d}t\right) = \frac{\beta_{z,g}}{\varepsilon_g}\tan\left(\beta_{z,g}(t-h)\right) \quad \textbf{(2.74)}$$

where

$$\beta_{z,d} = \sqrt{\beta_{d,\mathrm{res}}^2 - \beta_r^2} = \sqrt{\omega_{\mathrm{res}}^2 \mu_d \epsilon_d - \left(\frac{\chi_{mn}}{a}\right)^2} \quad \textbf{(2.75)}$$

$$\beta_{z,g} = \sqrt{\beta_{g,\mathrm{res}}^2 - \beta_r^2} = \sqrt{\omega_{\mathrm{res}}^2 \mu_g \epsilon_g - \left(\frac{\chi_{mn}}{a}\right)^2} \quad \textbf{(2.76)}$$

Eqn. 2.74 can be used to calculate the resonant frequency of a cavity with known dimensions. The presence of the dielectric insert changes the height-to-radius ratio of the cavity and as a result brings down the resonant frequency. Therefore, by varying the thickness of the dielectric one can change the resonant frequency to the desired range.

By choosing a resonant frequency between 14 and 14.5 GHz, the MET was sized to be 16.5 mm in diameter and 24.7 mm tall, with a 3-mm boron nitride dielectric cap.

CHAPTER 3

Optimization Studies

In order to transition the low power 14.5-GHz MET to a high power MET, three main optimization studies were performed. Research was done in the areas of antenna height, radio frequency (RF) inputs, and dielectric shapes to increase the performance of the MET.

3.1 Antenna Height Optimization

One of the important goals of the 14.5 GHz MET was to assure high coupling efficiency. Coupling efficiency is a performance value used to measure the amount of power absorbed by the plasma. It is calculated by using the forward power and reflected power measurements,

$$\text{Coupling Efficieny (\%)} = \frac{P_{\text{for}} - P_{\text{ref}}}{P_{\text{for}}} = \frac{P_{\text{inp}}}{P_{\text{for}}} \quad \textbf{(3.1)}$$

Since coupling efficiency is a function of the antenna height, a network analyzer was used to measure the absorbed power of the cavity at various antenna heights. Four different antenna heights ranging from 0.7 mm, 1 mm, 1.4 mm, and 2 mm were tested. The recorded antenna height was measured from the base of the MET to the tip of the antenna. The network analyzer was set to the S_{11} mode and the magnitude of dip at the resonant frequency for each antenna height was recorded, the results for which are shown in Table 3.1.

Table 3.1: Cavity's absorbed power at various antenna heights measured using a network analyzer

Antenna Height (mm)	*Absorbed Power (dBm)*
0.3	−22
0.7	−21
1.0	−10
1.4	−8.5
2.0	−4

As one can see, antenna protrusions between 0.3 mm to 0.7 mm resulted in the highest absorbed power and therefore provide the best coupling efficiency. As will be presented in Chapter 4, hot fire testing of the MET with antennas less than 0.7 mm resulted in coupling efficiencies as high as 96%.

3.2 RF Input Optimization

Due to the operational frequency range of the 14.5-GHz MET, the initial design of the RF inputs for the antenna and the waveguide transitions were done using a SMA coaxial connector. The SMA connectors were found to be extremely reliable under low power (<20 W) and provided good results. However, when tested under high power the SMA connectors were prone to frequent failures. Above 50 W, the epoxy material maintaining the vacuum seal of the connector broke down, thereby compromising the MET's vacuum as well the gas inside the MET (Figure 3.1).

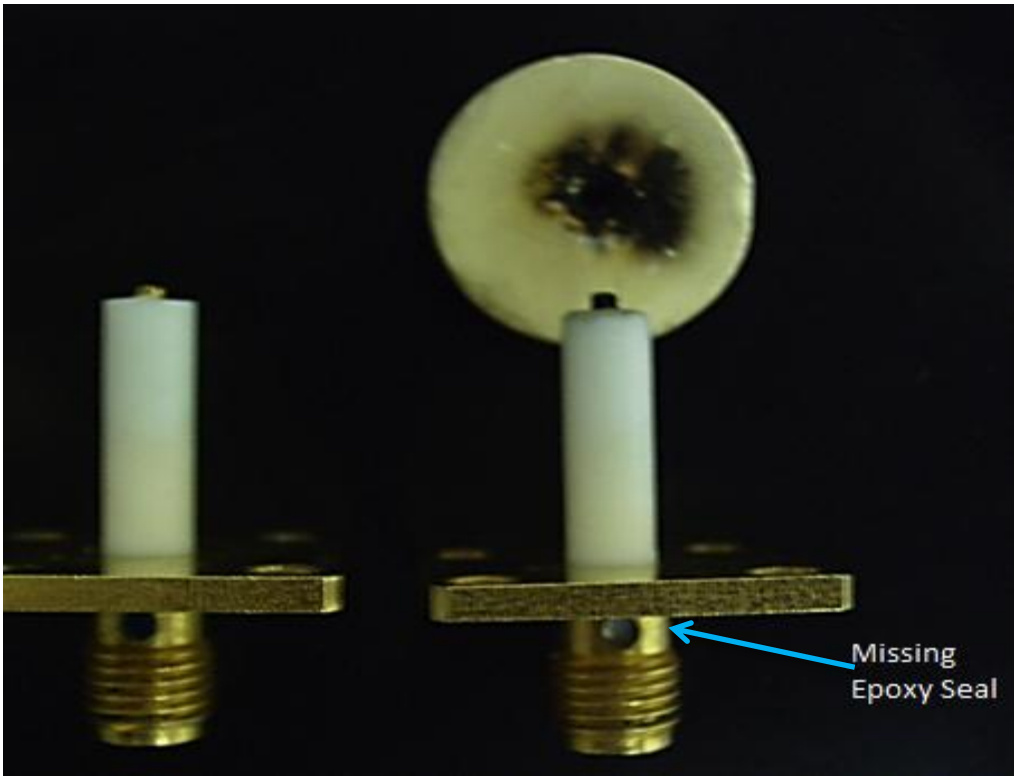

Figure 3.1: SMA antennas: (left) new SMA antenna; (right) damaged SMA antenna with charring at the bottom of the dielectric

As a result, the RF inputs were changed to use N-type connectors. Although, the N-type connectors were also susceptible to similar failures, it did raise the maximum possible forward power to 100 W.

3.3 Dielectric shape optimization

Proper sizing of the MET's dielectric insert was done using the equations presented in Section 2.2.3. The introduction of a dielectric insert reduces the cavity height-to-radius ratio and will thereby reduce the resonant frequency. Using values for a TM^{z}_{011} mode along with the cavity's dimensions, MATLAB was used to plot both sides

of Eqn. 2.74 to find the theoretical resonant frequency (Appendix A), the results of which are shown in Figure 3.2.

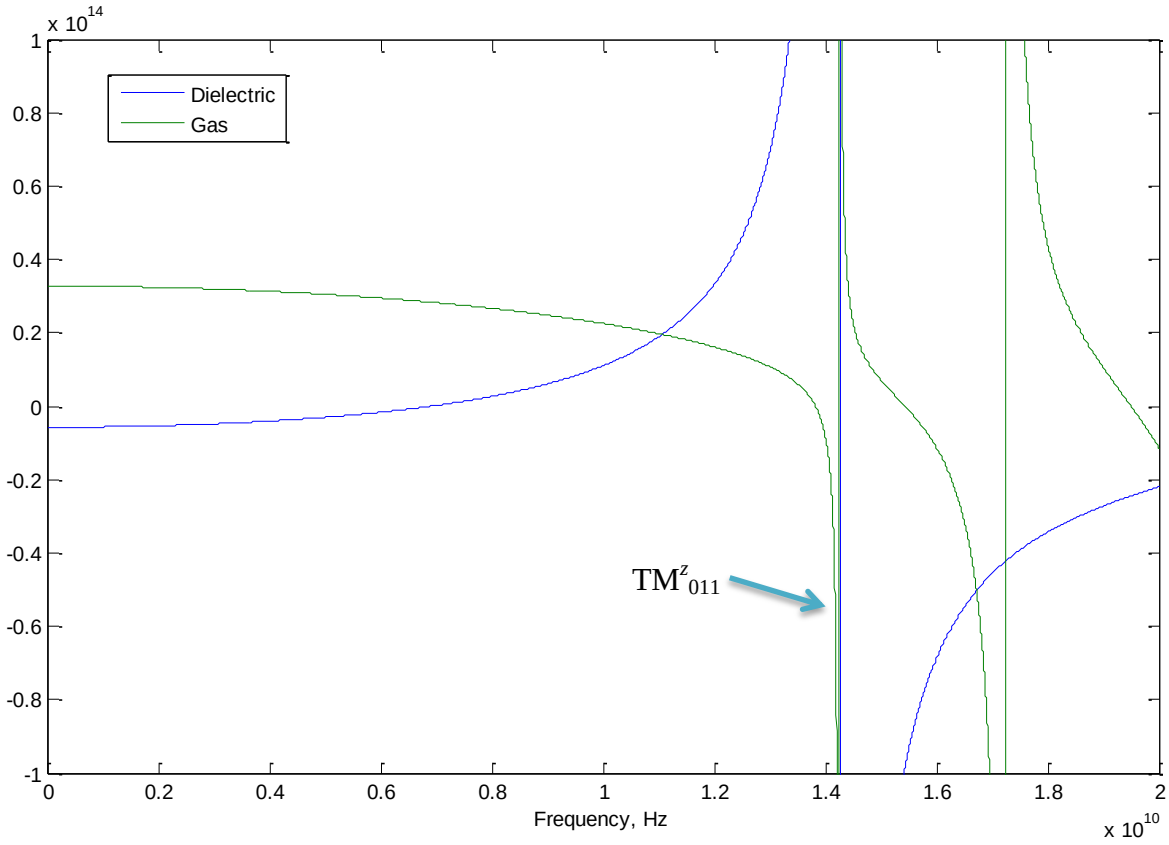

Figure 3.2: Theoretical resonant frequency calculations

The first point of intersection between the two lines represents the first transverse mode, TM^z_{010}, while the second point of intersection represents the second mode, TM^z_{011}, and so on. The actual resonant frequency can vary slightly due to propellant and geometric effects.

Initially, a cylindrically shaped dielectric cap was placed at the base of the MET, with a small hole drilled at the bottom to cover the protruding antenna tip. When this configuration was tested under high forward power, it resulted in significant amount of charring at the bottom of the dielectric as well as melting of the Teflon material

insulating the antenna (Figure 3.1). This was a direct result of the extremely high temperatures present at the tip of the antenna. Therefore, to counteract the extreme temperatures the Teflon material near the tip was removed and the ceramic dielectric was shaped around the tip of the antenna (Figure 3.3). This resulted in little to no charring being present when testing.

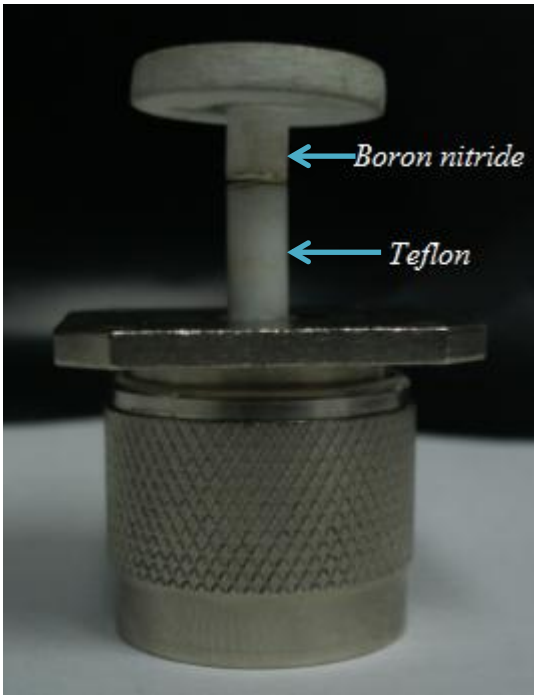

Figure 3.3: N-type antenna with Teflon insulator and dielectric cap shaped around the tip.

CHAPTER 4

Experimental Results

The main objective of this thesis is to advance on the work initially done by Goovaerts on the low power (<20 W) 14.5-GHz MET.[3] Testing of the MET was done using helium as the propellant and under a vacuum pressure to simulate the space environment.

4.1 Setup Overview

The experimental setup used for the testing of the 14.5-GHz MET consists of the cavity itself and various pieces of equipment used for microwave generation and propellant control. The microwave generation section consists of a microwave signal generator, a variable power traveling wave tube amplifier (TWTA), power sensors, and power meters. WR-75 waveguides were used throughout the setup for the transmission of electromagnetic waves. The propellant control section consists of a mass flow controller, feed lines, and a vacuum pump. A more detailed schematic of the setup is shown in Figures 4.1 and 4.2.

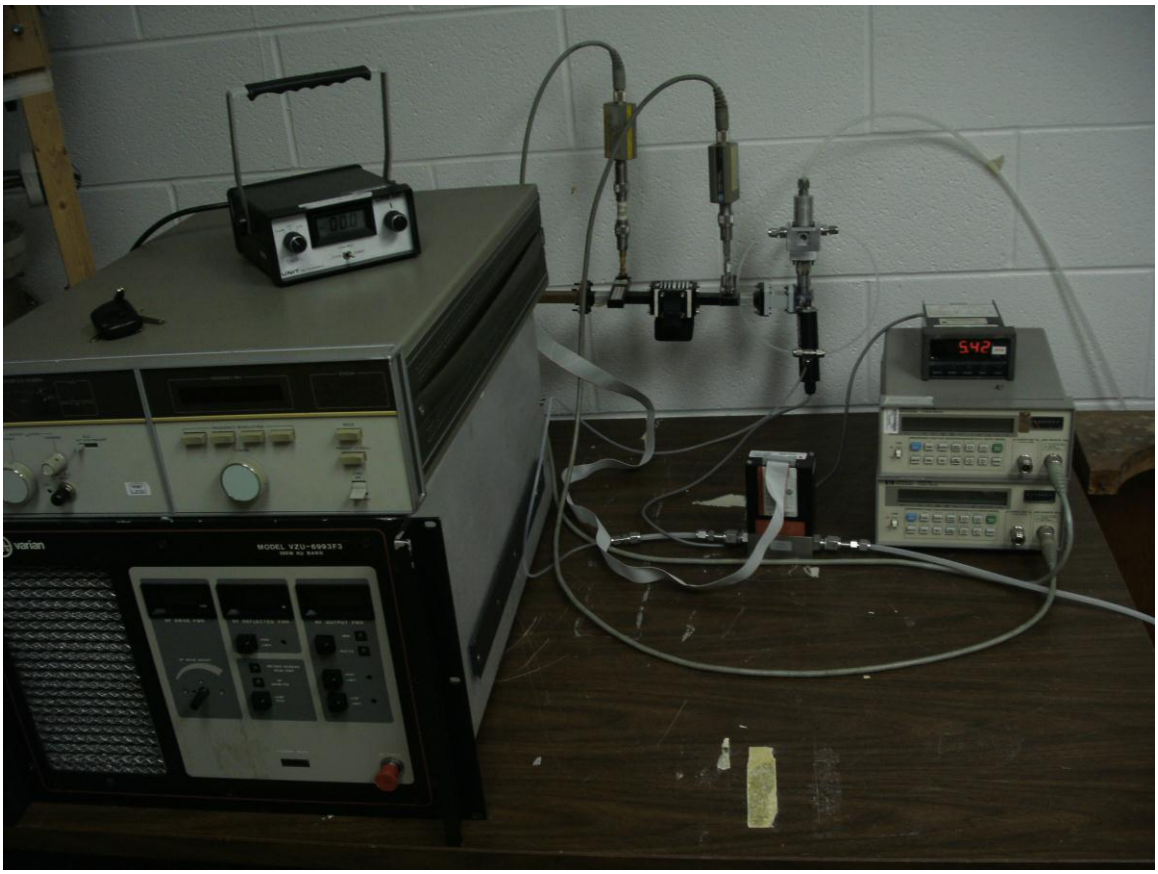

Figure 4.1: Experimental setup used for the testing of high power 14.5 GHz MET

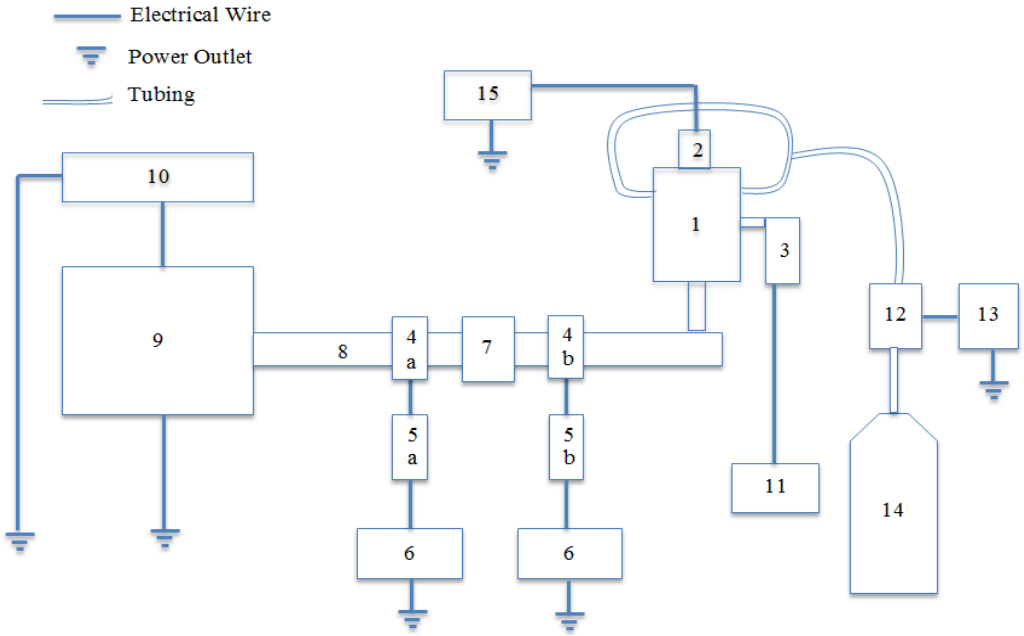

Figure 4.2: Detailed schematic of the experimental setup

1. 14.5-GHz high power microwave electrothermal thruster
2. Vacuum chamber attachment
3. Omegadyne pressure transducer,
4. (a) Advanced Microwave Components waveguide crossguide coupler, AMC-CGC, WR-75, 40.35-dB gain at 14.5 GHz; (b) Advanced Microwave Components waveguide crossguide coupler, AMC-CGC, WR-75, 40.50-dB gain at 14.5 GHz
5. (a) Hewlett Packard power sensor, HP 8481A; (b) Hewlett Packard power sensor, HP 8481D
6. Hewlett Packard power meters, HP 437B
7. Apollo Isolator, WR-75
8. WR-75 waveguide attachment
9. Varian 300 W Ku Band TWTA, VZU-6993F3
10. Hewlett Packard 2–18 GHz CW signal generator, HP 8671B
11. Omega pressure meter
12. Tylan mass flow controller, FC-2900V
13. Unit Instruments mass flow controller meter and power supply, URS-20
14. Helium propellant tank
15. Vacuum pump

4.2 Operational Procedures

The MET was tested under two operating conditions, cold flow and hot fire. The data obtained under these conditions was used to characterize the performance of the MET.

4.2.1 Cold Flow Procedure

Cold flow testing of the MET was done using a 0.0059-inch constant diameter nozzle, and helium as the propellant. First, the cavity was pumped down as close to vacuum pressure as possible. Following a leak check procedure, the propellant was injected into the cavity with increasing mass flow. Since, the mass flow controller used for this experiment was initially designed for using with nitrogen, proper calculations were made to recalibrate it for helium. The chamber pressure at each increment of mass flow was recorded. The cold flow chamber pressure will be used in conjunction with the hot fire data to derive the theoretical values of thrust and specific impulse for the MET.

4.2.2 Hot Fire Procedure

Once a cold flow procedure was completed, the cavity was once again pumped down to a vacuum pressure. A small amount of propellant was then fed into the system to evacuate the remaining air and fill it with propellant. Next, continuous wave microwave energy, at a resonant frequency of 14.24 GHz, was introduced into the system. At these conditions the chamber pressure was low enough (~5 kPa) for an electric breakdown of the gas, and as a result a plasma was ignited. Mass flow was then raised at incremental rates along with forward power. The chamber pressure, forward power, and reflected power were recorded at each mass flow increment.

Although two different coaxial inputs were tested, the operational procedures under cold flow and hot fire were the same. Due to the functional limit of the coaxial inputs, the forward power was limited to 100 W for the N-type connector.

Figure 4.3: MET firing into a vacuum chamber attachment

4.3 Thruster Performance Data

The performance of the MET was characterized based on the experimental and theoretical values obtained from testing. Performance data relating to thrust and specific impulse were obtained through equations detailed in Chapters 1 and 2.

4.3.1 Cold Flow Testing Results

Prior to any hot fire testing, cold flow measurements of chamber pressure and mass flow rate were taken for comparison with hot fire results. Measurements were taken over a period of two days to show repeatability as well as accuracy of the data. Results are shown in Figure 4.4.

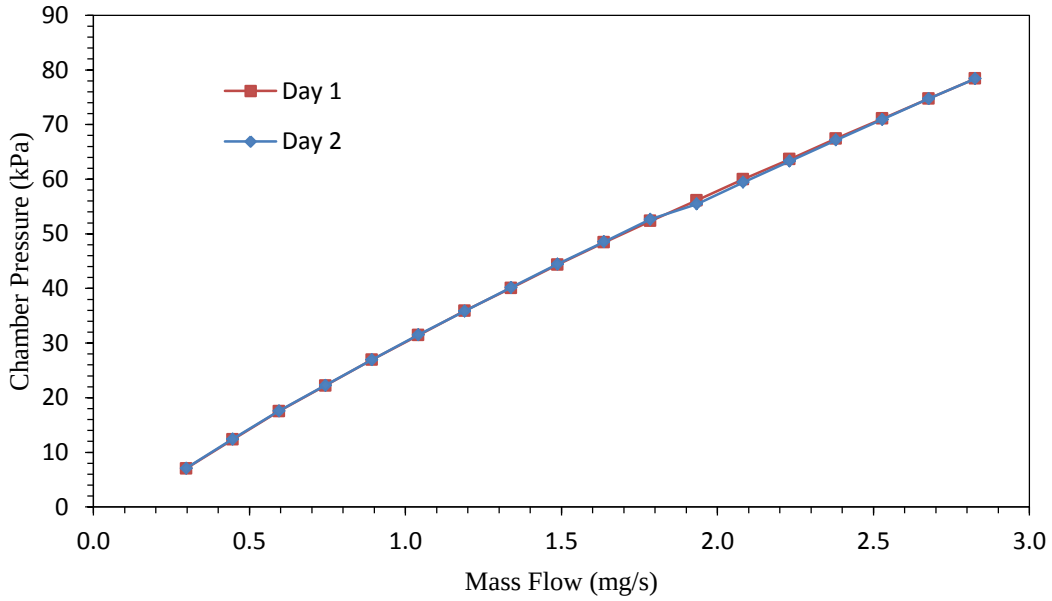

Figure 4.4: Cold flow chamber pressure versus mass flow rate. Propellant is helium.

As Figure 4.4 illustrates, the data taken over the two days virtually overlap each other, indicating good data repeatability. Furthermore, there is a good linear trend between mass flow and chamber pressure, as expected. Using the data in Figure 4.4, the nozzle's discharge coefficient was calculated and plotted in Figure 4.5. With increasing mass flow rate the boundary layer displacement thickness decreases causing the coefficient of discharge to increase. The curve levels off at around 0.5 indicating that the boundary layer occupies a significant area of the nozzle.

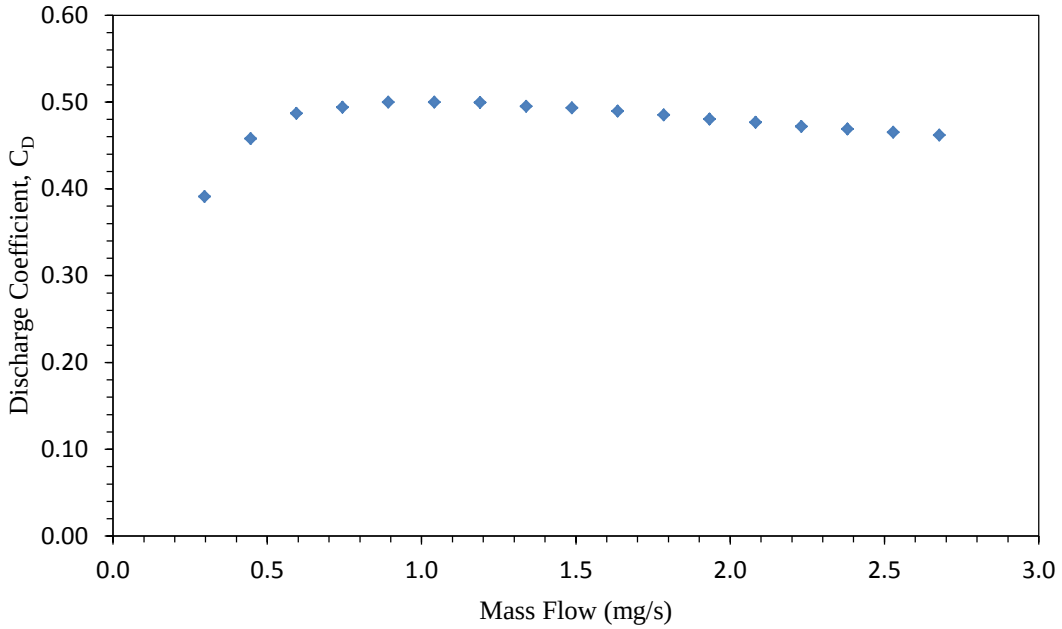

Figure 4.5: Discharge coefficient versus mass flow rate. Propellant is helium.

The experimental values of chamber pressure were plugged into Eqn. 2.17 to obtain theoretical values of thrust. The exit pressure was obtained through Eqn. 2.8, where the cold flow chamber pressure was plugged in as the stagnation pressure, and the exit Mach number was assumed to be 1. As shown in Figure 4.6, the values of thrust increase in relation to an increasing mass flow rate. The maximum value of thrust obtained was 9.56 mN at a mass flow rate of 2.83 mg/s of helium. Higher values of thrust will be expected under hot fire conditions due to the increase in chamber temperature which will thereby increase the chamber pressure.

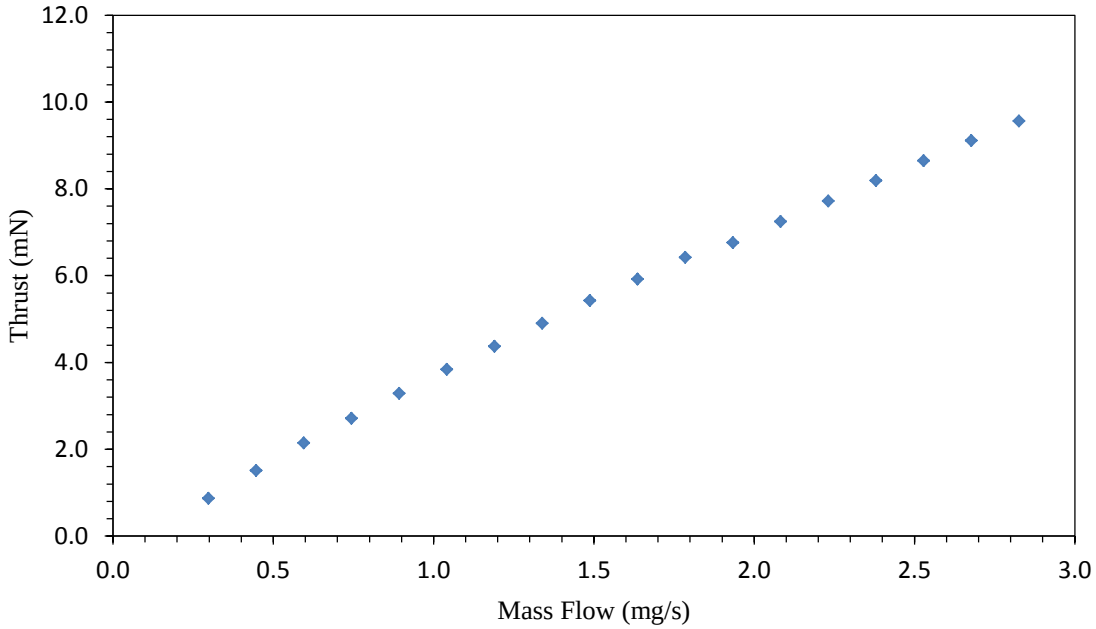

Figure 4.6: Cold flow ideal thrust versus mass flow rate. Propellant is helium.

4.3.2 Hot Fire Testing Results

Following a cold flow run on day 2, a hot fire experiment was performed. During the hot fire run values of chamber pressure, mass flow rate, forward power and reflected power were recorded. Using Eqn. 3.1, values of forward power and reflected power were plugged in to obtain the input power and coupling efficiency. Furthermore, values of specific power ($P_{inp}/\dot{m}$), and ratio of hot chamber pressure to cold chamber pressure were also calculated for plotting.

The forward power of the cavity was increased at a steady rate from 20 W to 96 W. During this time the reflected power also steadily grew from 1 W initially, to 25 W at the final mass flow increment. Plots of the cavity's input power at the corresponding mass flow rate, and chamber pressure are displayed in Figure 4.7 and 4.8, respectively.

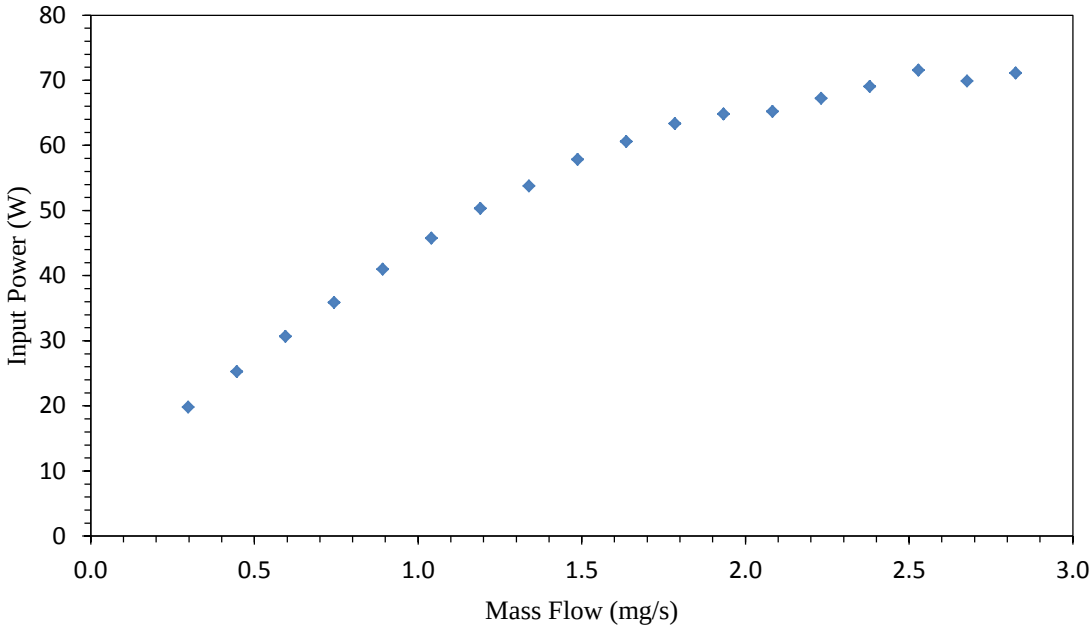

Figure 4.7: Input power versus mass flow rate. Propellant is helium.

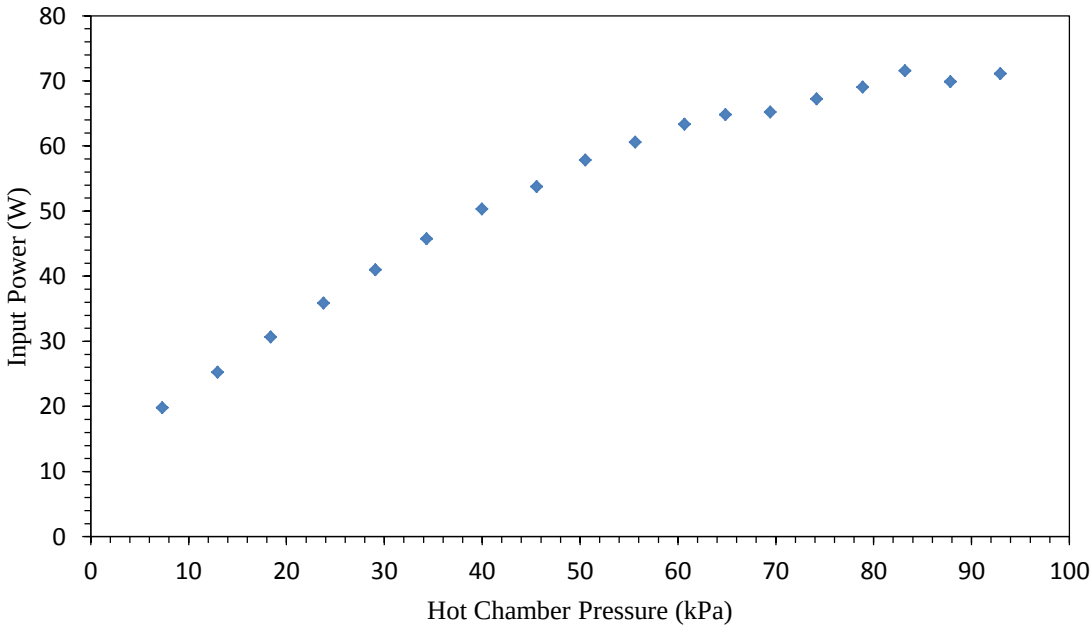

Figure 4.8: Input power versus hot fire chamber pressure. Propellant is helium.

The input power steadily grew as the forward power was increased while reaching a peak input power of 71 W. While input power was in the range of 19–71 W, coupling efficiency as high as 96% was recorded. The behavior of the coupling efficiency as a function of the forward power is displayed in Figure 4.9. Following initial plasma ignition, the coupling efficiency stayed in the mid-90% range and begins to decline starting at 70 W of forward power. Poor coupling efficiency can result from an impedance mismatch and could be the reason for low coupling efficiency here as well. The cause of the mismatch could possibly stem from the change in permittivity of free space inside the cavity following the ignition of the plasma. 70 W is close to the functional limit of the antenna and could be the beginning point for the breakdown of the insulating Teflon material. The broken down material can mix with the gas inside the cavity changing the permittivity.

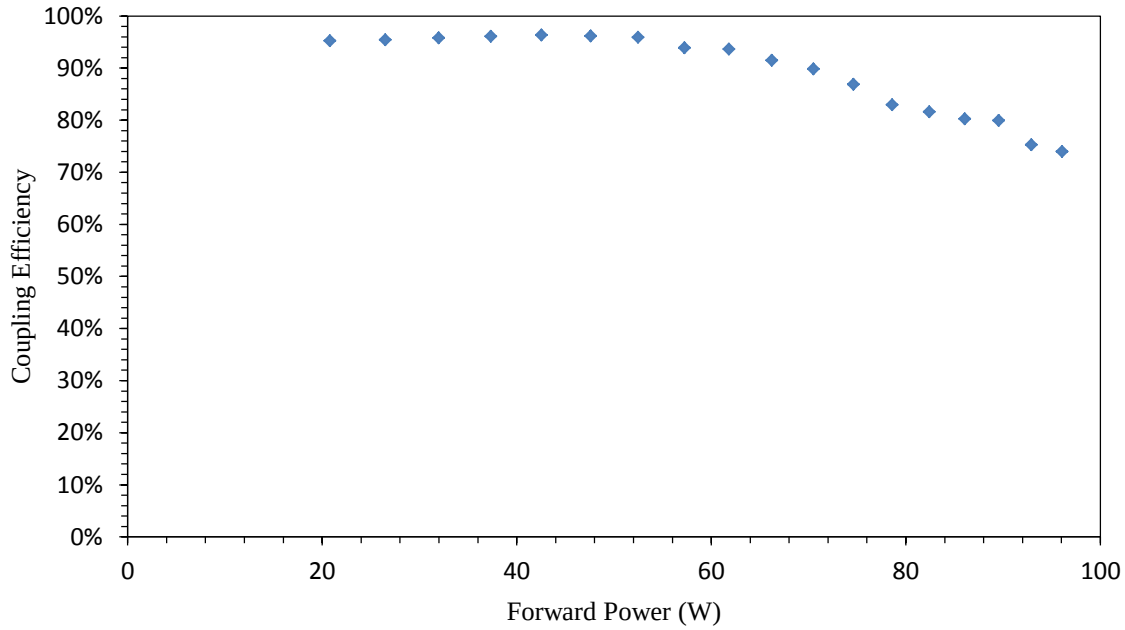

Figure 4.9: Coupling efficiency versus forward power. Propellant is helium.

The recorded hot fire chamber pressure values were plotted as a function of mass flow rate and specific power in Figures 4.10 and 4.11, respectively. The hot fire chamber pressure increased linearly with an increasing mass flow rate and decreased exponentially with an increasing specific power. Since the mass flow controller used for this experiment was limited to a maximum flow rate of 2.83 mg/s, a peak chamber pressure of 92 kPa was achieved. However, previous experiments with larger mass flow controllers resulted in stable plasma being sustained at chamber pressures as high as 110 kPa.

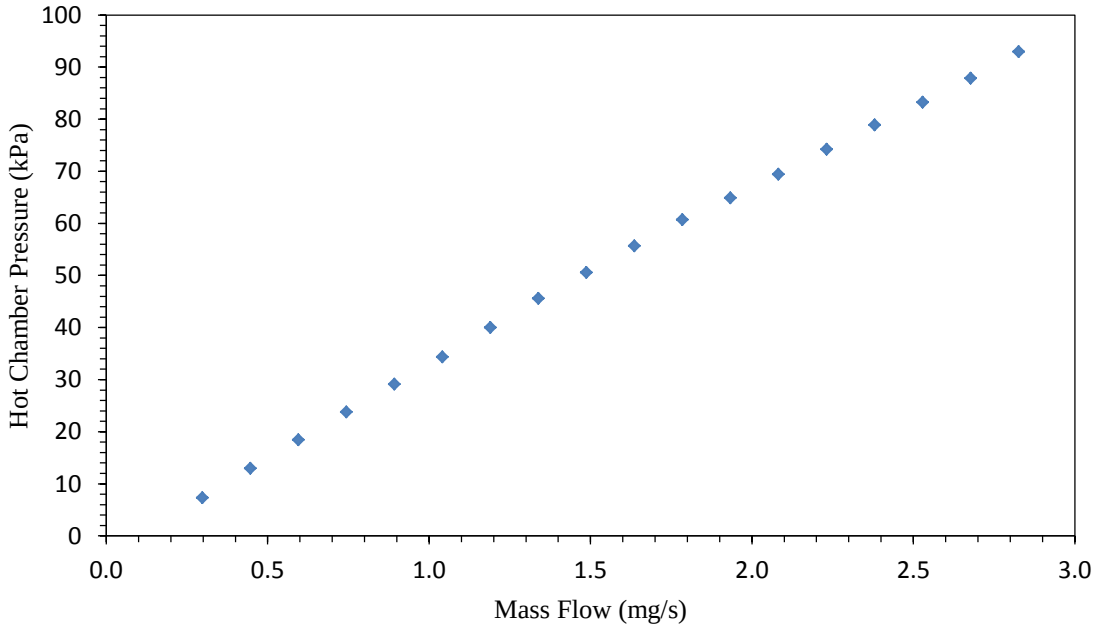

Figure 4.10: Hot fire chamber pressure versus mass flow. Propellant is helium.

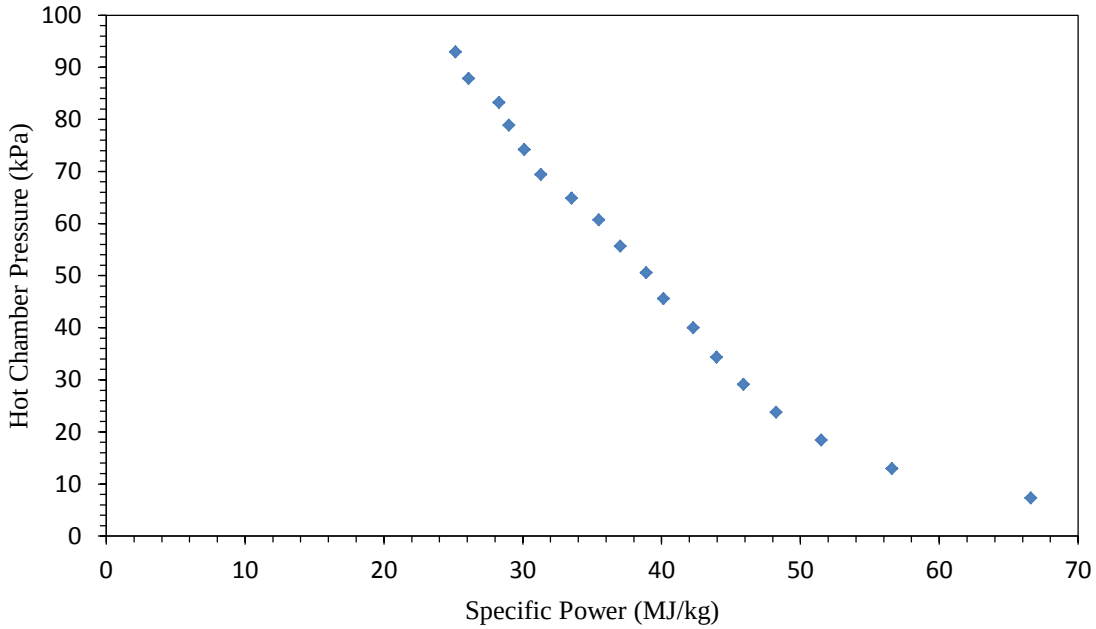

Figure 4.11: Hot fire chamber pressure versus specific power. Propellant is helium.

The hot fire chamber pressures were plotted against cold flow chamber pressures in Figure 4.12. In addition, the ratios of hot fire chamber pressure to cold flow chamber pressure were plotted as a function of mass flow rate in Figure 4.12. Based on the linear increase of the pressure ratios in Figure 4.13, one would expect the data in Figure 4.12 to exhibit an increasing slope. However, due to lack of data at higher mass flow rates it cannot be illustrated. Currently, the cold flow chamber pressure shows a linear fit against the hot fire chamber pressure, indicating that it could be the lower end of the curve. Previous 7.5 GHz and 2.45 GHz METs were able to attain maximum pressure ratios around 3. Therefore, it is conceivable to expect much higher pressure ratios if mass flow rate was significantly increased. However, in comparison to Goovaerts' low power MET, the high power MET was able to attain higher pressure ratios at similar mass flow rates.

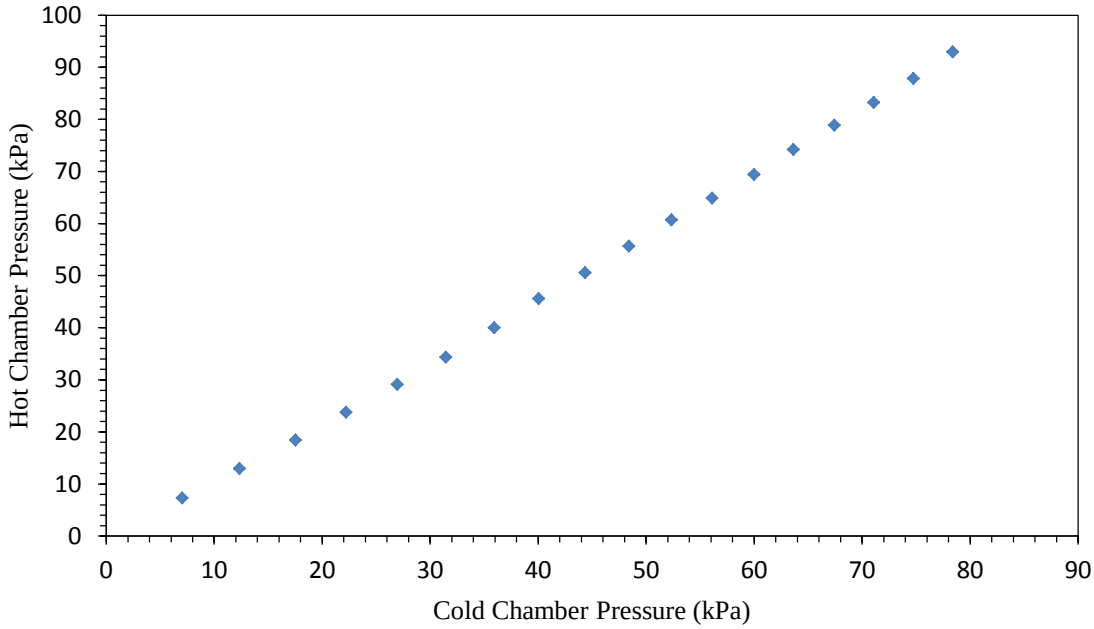

Figure 4.12: Hot fire chamber pressure versus cold flow chamber pressure. Propellant is helium.

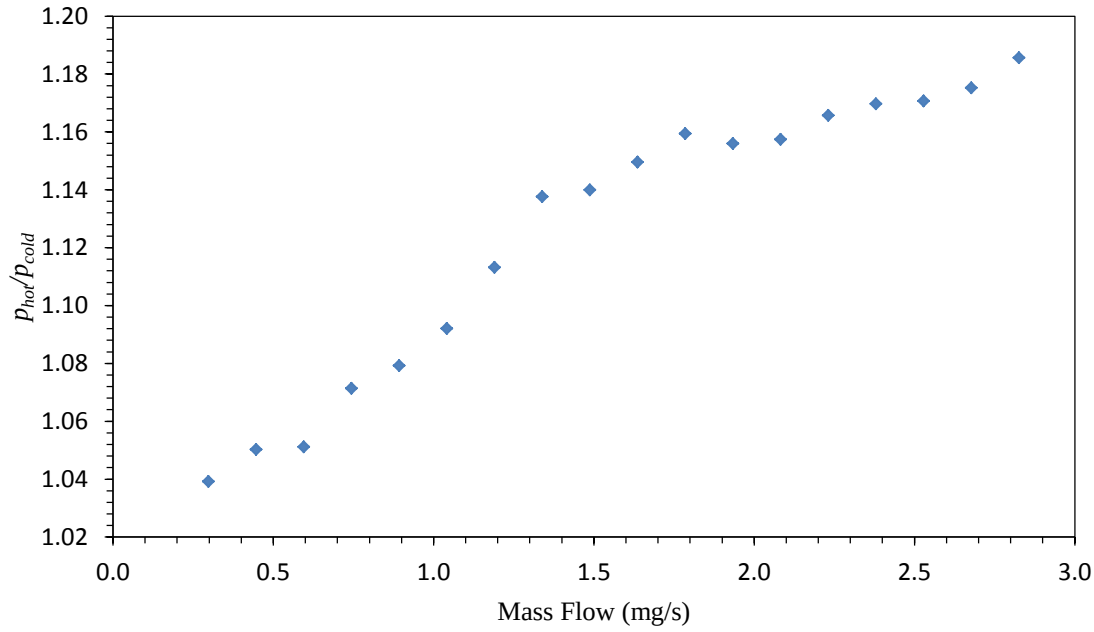

Figure 4.13: Ratio of hot fire chamber pressure to cold flow chamber pressure versus mass flow rate. Propellant is helium.

4.3.3 Theoretical Interpretation of Hot Fire Testing

Theoretical values of thrust and specific impulse were derived through the combination of isentropic flow relations detailed in Chapter 2, and Eqns. 1.5 and 1.8. They were calculated assuming an ideal converging only nozzle. Values for chamber temperatures were calculated using Eqn. 2.25. These values were plotted as a function of mass flow rate, specific power, and hot chamber pressure in Figures 4.14, 4.15, and 4.16, respectively. During the experiment chamber temperatures as high as 411 K were recorded, and its behavior relative to mass flow rate can be broken down into two half sections. The slope of the curve in the first half is much steeper compared to the slope in the second half of the curve. The decrease in the rise of chamber temperature could be attributed to the lack of input power required to heat the propellant.

Values of thrust were plotted as a function of mass flow rate and specific power in Figures 4.17 and 4.18, respectively. Thrust increased with increasing mass flow rate and ranged between 0.9–11.33 mN. However, when compared to the graph of specific impulse versus mass flow rate in Figure 4.19, it is important to note that the highest specific impulse did not occur at the highest thrust value. Values of specific impulse ranged between 305–423 s; however, its behavior was unexpected. Instead of a steady increase with increasing mass flow rate, specific impulse seems to level out at a flow rate of 1.64 mg/s and begins to decrease. Since specific impulse is a function of chamber temperature, the decrease in specific impulse can be attributed to the decrease in rate of chamber temperature increase in the latter half of the graph.

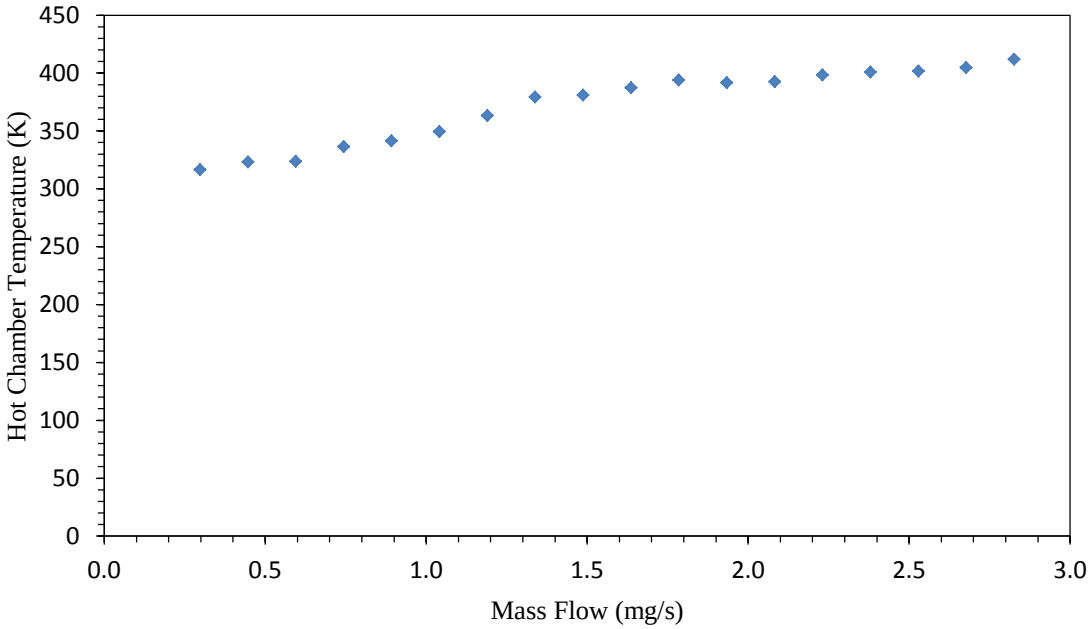

Figure 4.14: Hot fire chamber temperature versus mass flow rate. Propellant is helium.

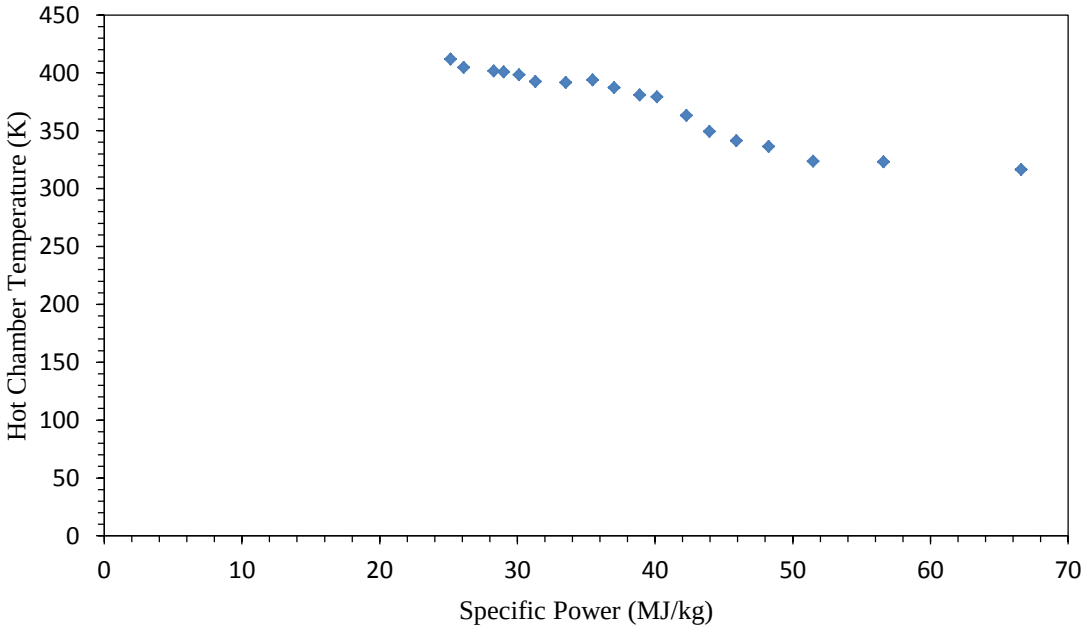

Figure 4.15: Hot fire chamber temperature versus specific power. Propellant is helium.

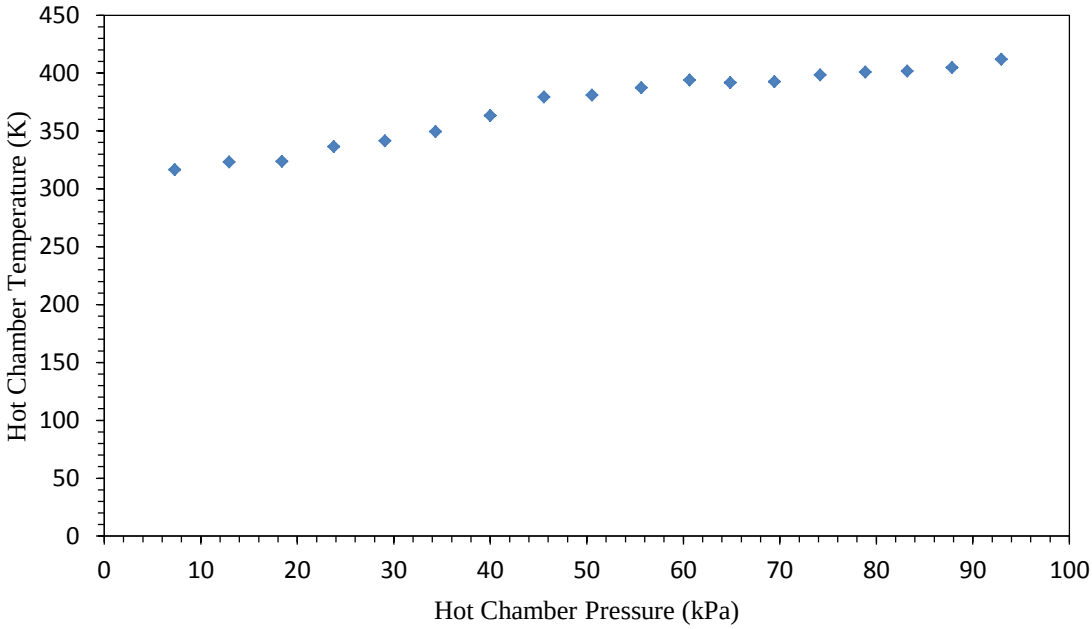

Figure 4.16: Hot fire chamber temperature versus hot fire chamber pressure. Propellant is helium.

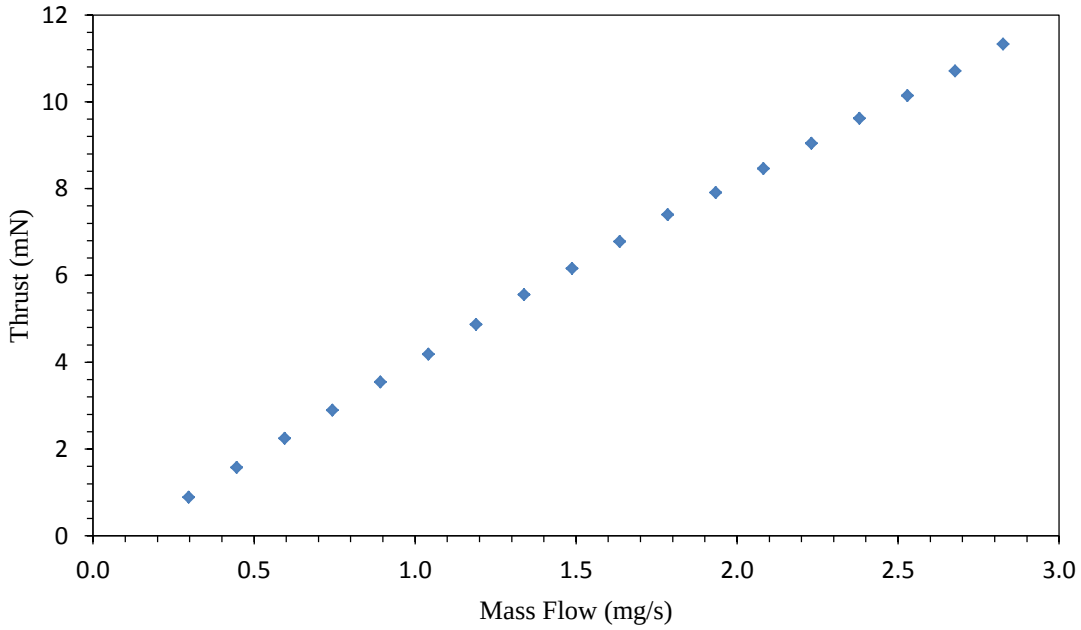

Figure 4.17: Hot fire thrust versus mass flow rate. Propellant is helium.

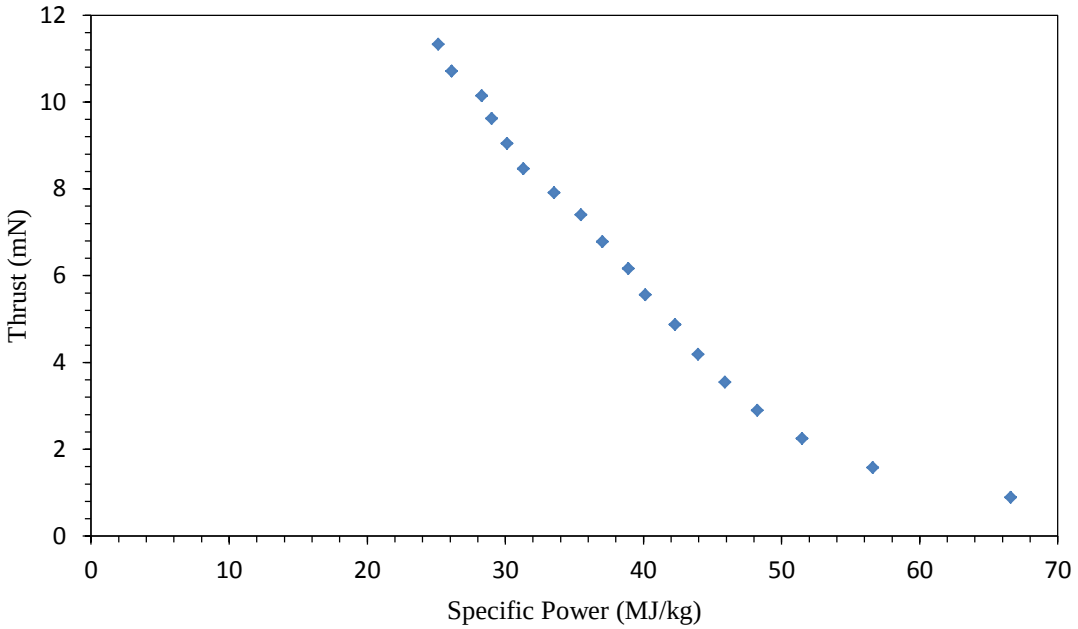

Figure 4.18: Hot fire thrust versus specific power. Propellant is helium.

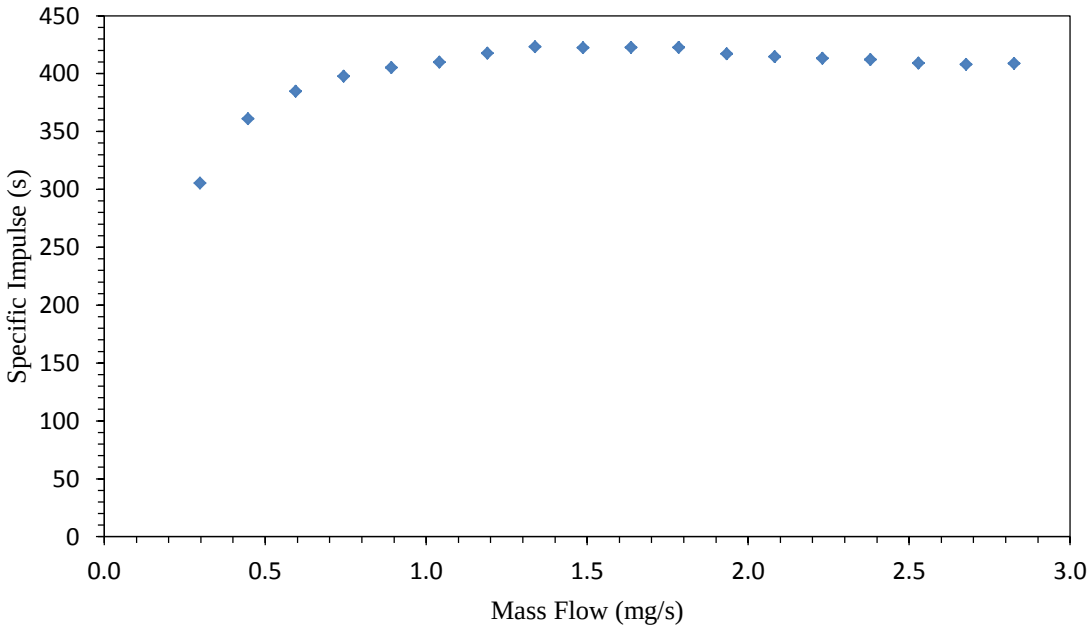

Figure 4.19: Hot fire specific impulse versus mass flow rate. Propellant is helium.

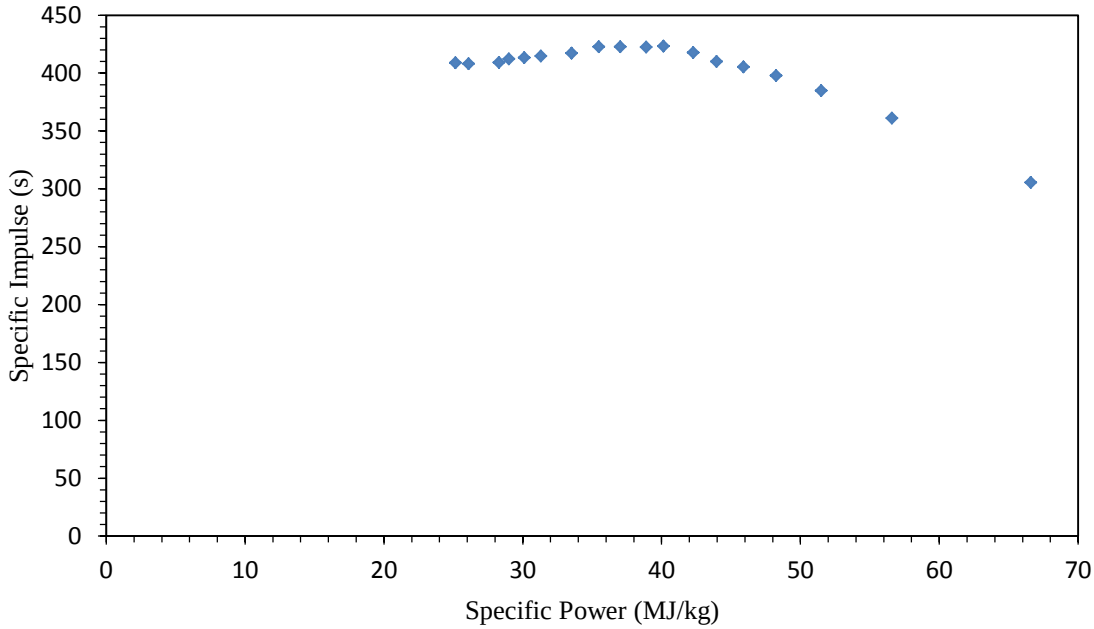

Figure 4.20: Specific impulse versus specific power. Propellant is helium.

CHAPTER 5

Conclusion and Recommendations

The objective of this research was to advance on the work previously done on the low power 14.5-GHz MET by Gooverts.[12] As part of the progression the low power solid state amplifier was replaced with a variable high power TWTA. Furthermore, changes were made in the areas of antenna design and dielectric shapes to incorporate functionality under the new high power requirement. The results of these changes lead to a total increase of 80 W in the forward power of the MET. Although the full potential of the 300-W TWTA could not be utilized, significant strides were made to make the MET functional at 100 W. Furthermore, problems encountered by Goovaerts, such as plasma ignition and plasma ascension,[3] were addressed and resolved in the design of the high power MET. The increase in forward power and reduction of the dielectric thickness lead to plasma that ignites instantly without the use of a tungsten wire, and a plasma that is located very close to the nozzle.

The results obtained from the testing of the high power MET showed significant improvements when compared to the low power MET. The addition of 80 W in forward power resulted in higher chamber pressures, and higher chamber temperatures. Consequently the maximum thrust attained increased from 4.2 mN to 11.33 mN, along with a 225 s increase in the highest specific impulse. However, the behavior of the data did not tend towards the expected when the forward power was increased past 70 W. Although the overall trend of the data continued to increase, the rate of increase began to decline. For example, coupling efficiency started to decline beginning at about 70 W. As

a result, less and less forward power was going towards heating of the plasma; therefore; chamber pressures and chamber temperatures data began to deviate from the expected. This could be the result of an impedance mismatch caused by reaching the functional limit of the N-type antenna. The N-type antenna proved to be improvement over the previous SMA connectors; however, they were also prone to similar failures but at a higher power.

Based on the analysis of the observations and acquired data, changes can be made to further increase the functional range of the high power MET. The main limiting factor through the testing process has been primarily the RF input. Therefore, the main priority in the future evolution of the MET would have to be choosing an RF input that can handle the full 300 W of the TWTA, if this is indeed possible. Other connectors, such as SC and TNC incorporate materials that can handle high amounts of power but may only be one part of the solution. The main cause for failure at high powers is the concentration of extreme temperatures due to heating at the tip of the antenna. Therefore, by increasing the diameter of the antenna, heat can be more easily dissipated. A combination of a better RF input with a large diameter antenna could be a solution; however; such a product may not be readily available for purchase from a vendor. Ultimately, a custom-built antenna and waveguide transition by integrating various off-the-shelf products might be the solution. Along the way, the MET will have to be modified to incorporate the various mounting holes and changes in antenna diameter.

Other immediate changes that can made to get better results would to use a larger flow rate mass flow controller. The current mass flow controller was limited to about 3 mg/s of helium. Therefore, increasing the mass flow rate can lead to higher chamber

pressures and higher values of thrust. Increasing the size of the injectors, along with propellant tubes, would further aid in increasing the mass flow limit of the MET. The addition of more mass flow would in turn require more power as well to heat the propellant. Therefore, changes to mass flow rate and RF inputs will have to done in step with each other.

References

1. Hill, P. G., and Peterson, C. R., *Mechanics of Thermodynamics of Propulsion*, 2nd edition, Addison-Wesley Publishing Company, Inc., New York, 1992.

2. Humble, R. W., Henry, G. N., and Larson, W. J., editors, *Space Propulsion Analysis and Design*, McGraw-Hill Companies, Inc., New York, 1995.

3. Goovaerts, K. M., Bilén, S. G., and Micci, M. M., "Design and Initial Testing of a Miniature Microwave Electrothermal Thruster (MiniMET)," AIAA-2007-5293, 43rd AIAA/ASME/SAE/ASEE Joint Propulsion Conference & Exhibit, Cincinnati, OH, 8–11 July, 2007.

4. Sullivan, D.J., *Development and Performance Characterization of a Microwave Electrothermal Thruster*, Master of Science Thesis, Department of Aerospace Engineering, The Pennsylvania State University, 1995.

5. Kline, J.F., *Thrust Measurements of a Microwave Electrothermal Thruster*, Master of Science Thesis, Department of Aerospace Engineering, The Pennsylvania State University, 1996.

6. Nordling, D., Souliez, F., and Micci, M. M., "Low-Power Microwave Arcjet Testing," AIAA-1998-3499, 34th AIAA/ASME/SAE/ASEE Joint Propulsion Conference and Exhibit, Cleveland, OH, 13–15 July 1998.

7. Nordling, D. A., *High-Frequency, Low-Power Microwave Arcjet Thruster Development*, Master of Science Thesis, Department of Aerospace Engineering, The Pennsylvania State University, 1998.

8. Souliez, F. J., *Low-Power Microwave Arcjet Spectroscopic Diagnostics and Performance Evaluation*, Master of Science Thesis, Department of Aerospace Engineering, 1999.

9. Roos, C. J. A., *Vertical Deflection Thrust Stand Measurements of a Low Power Microwave Arcjet Thruster*, Master of Science Thesis, Department of Aerospace Engineering, The Pennsylvania State University, 2001.

10. Welander, B. A., *Low Power Microwave Arcjet Thruster Using Nitrogen Propellant*, Master of Science Thesis, Department of Aerospace Engineering, The Pennsylvania State University, 2004.

11. Clemens, D. E., *Performance Evaluation of a Low-Power Microwave Electrothermal Thruster*, Master of Science Thesis, Department of Aerospace Engineering, The Pennsylvania State University, 2004.

12. Goovaerts, K. M., *Feasibility Studies of a 14.5-GHz, Low Power Microwave Electrothermal Thruster*, Master of Science Thesis, Department of Aerospace Engineering, The Pennsylvania State University, 2007.

13. Blum, J. H., *Performance Evaluation and Optimization of an 8-GHz Microwave Electrothermal Thruster*, Master of Science Thesis, Department of Aerospace Engineering, The Pennsylvania State University, 2009.

14. Balanis, C.A., *Advanced Engineering Electromagnetics*, John Wiley & Sons, Inc., Hoboken, 1989.

APPENDIX A

MATLAB Code

```
%Rohit Adusumilli
%Mini-MET Resonant Frequency calculations
clear all
clc

a = 8.25e-3;
h = 27.7e-3;
t = 3e-3;
eg = 8.854e-12;
mu = 1.25664e-6;
ed = 4*eg;
x01 = 2.4049;
x11 = 3.8317;
f = linspace(0,2e10,10000);
c1 = (2*pi)^2;
cd = mu*ed;
cg = mu*eg;

betaR = x01/a;

betad = sqrt((c1*(f.^2)*cd)-(betaR.^2));
betag = sqrt((c1*(f.^2)*cg)-(betaR.^2));

l = tan(betad*t);
m = betad/ed;
p = betag/eg;
q = tan(betag*(t-h));

for i=1:10000
    y(i) = l(i)*m(i);
    z(i) = p(i)*q(i);
end


plot(f,y,f,z)
axis([0 2e10 -1e14 1e14])
xlabel('Frequency, Hz')
legend('Dielectric','Gas')
```